Master's Thesis

Biosensors based on Novel Material Field Effect Transistors

Written by

Gernot Fleckl

to fulfill the requirements for assignment of the degree

Diplomingenieur

at

Technische Universität Wien

Supervised by

Prof. Franz Keplinger

Co-supervised by

Prof. A.T. Charlie Johnson

Eidesstattliche Erklärung

Ich erkläre hiermit an Eides statt, dass ich meine Diplomarbeit nach den anerkannten Grundsätzen für wissenschaftliche Abhandlungen selbstständig ausgeführt habe und alle verwendeten Hilfsmittel, insbesondere die zugrunde gelegte Literatur, genannt habe.

Wien am 10.06.2016

Acknowledgement

This research stay at Universtiy of Pennsylvania was funded by

Abstract

For different purposes, state-of-the-art antigen detection mechanisms like ELISA are not sufficient in accuracy. Therefore, new approaches have to be developed to get highly sensitive technologies. Graphene's outstanding electrical properties, like ultrahigh charge mobility and sensitivity to dopants, make it to a promising candidate for new electronic devices and their utilization for sensing technologies. Recent progress in nanotechnology has enabled new possibilities and, thus, has allowed the construction of graphene field effect transistors (gFET). In this work, gFET arrays with high yield and good device-to-device characteristic have been fabricated. Siliconoxide (SiO_2) and aluminiumoxide (Al_2O_3) have been used as insulating oxide layers. To utilize the gFET device, a chemical linker was attached by $\pi - \pi$ stacking interactions. The linker himself binds antibody fragments, so called single chain variable fragments (scFv). In this approach, detection of HER3, a well known breast cancer biomarker, was of interest. Therefore, matching HER3 immunoglobulin G-antigen complexes were used. Conclusions about the concentration of HER3 antigens down to as small as ng/ml were deducible by monitoring the Dirac voltages of the gFET devices.

Contents

1 Introduction

The modern semiconductor technologies have opened a wide range of technological purposes in many subject areas. The proceedings in nanotechnologies, like the discovery of carbon nanotubes in 1991 by Iijima [1] and the exfoliation of graphene in 2004 by Novoselov [2], have enabled experimental research on carbon based materials. These succeded in the application of these materials in field effect transistors with both, carbon nanotube and graphene channels. Transistors with novel materials as a gate channel might overcome the issues and associated limitations which occur with the ongoing shrinking of dimensions, like drain induced barrier lowering. However, it is of interest to achieve better device characteristics, like low capacity and high switching speed. Recent advances in production of graphene [3] [4] have enabled big scale growth of graphene on copper foils. Hence, new process procedures for graphene field effect transistor (gFET) fabrication have been enabled. Fabrication of gFET arrays are possible and their electrical characterization can be done simultaneously. Arrays with comparable device-to-device characteristic and with a high yield can be build.

Beside the application of nanomaterials in devices with electrical or mechanical use, there is an ambitious and promising use of nanomaterials for biological purposes. [5] [6] [7] [8] These materials have dimensions in the range of biological entities. As illustrated in figure 1.1, viruses have the same magnitude as the channel of common MOS transistors, nanowires are comparable to proteins and carbon nanotubes (CNTs) have the same diameter as the helical structure of DNA. The comparable length scales of solid state carbon materials and the biological entities enable physical interaction. Therefore, the study of biological interactions can be done, for example the acquisition of real time data of conformational changes in a biomolecule and may enable better
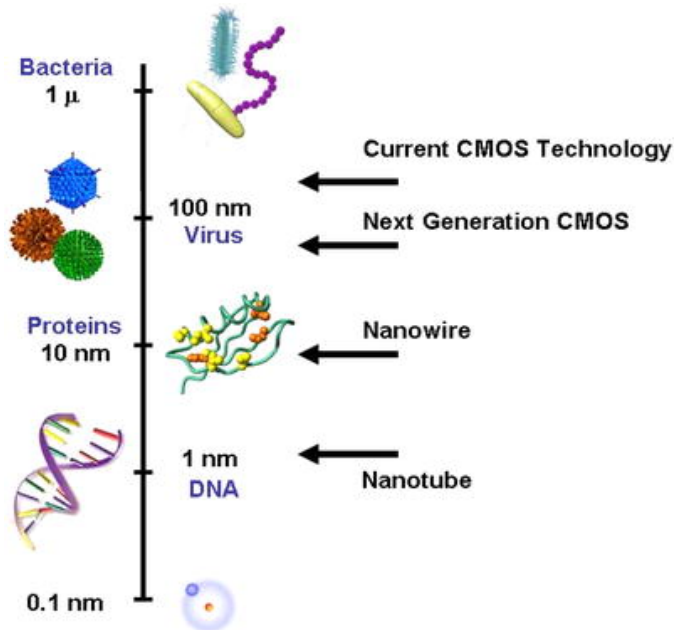
Figure 1.1: Size comparison of state of the art technology and biological entities. Figure from [8].

understanding of biological processes.

There is a need of high sensitive and quick sensors for detection of chemical compounds, like biological entities or explosives. Such devices could be used as point of care (PoC) medical devices or for quick and reliable security checks at airports. The idea of PoC-systems is the use of a hand-held device combined with detachable, single use chips with arrays of readout-devices. The hand-held device manages the readout and the interpretation of the electrical characteristic. PoC-tools embody a big step in the evolution of health care diagnosis, accelerates the everyday in clinical environments and makes life of chronically ill people easier. Most recently it enables new opportunities to people in developing countries because this technology is comparable cheap, easy to use and has low demands in the environment. Thus, it's well suited to be deployed in a rough environment.

2 Graphene

2.1 General Structure and Bandstructure

Graphene is a two-dimensional, one atom thick layer of sp^2 bonded carbon atoms and has a honeycomb lattice as shown in figure 2.1. It's the building material of different derivations of carbon materials. As shown in 2.2, fullerenes and carbon nanotubes are constructed out of graphene. If you stick several layers of graphene together, you obtain graphite. The inverse process was used by Novoselov and Geim in [2] by mechanical exfoliation of graphene from Highly Ordered Pyrolytic Graphic (HOPG). A unit cell of graphene contains two carbon atoms. The appropriate unit cell vectors are

$$a_1 = a_0\sqrt{3}\Big(\frac{1}{2}, \frac{\sqrt{3}}{2}\Big) \tag{2.1}$$

$$a_2 = a_0\sqrt{3}\Big(-\frac{1}{2}, \frac{\sqrt{3}}{2}\Big) \tag{2.2}$$

with an distance $a_0 = 0.142nm$ between two adjacent carbon atoms. A carbon atom has two electrons in the valence band ($1s^2 2s^2 2p^1 2p^1$) in its basic state. The sp^2 hybridization orbital uses two $2p$ orbitals and the preferable direction is a triangular-planar shape. The preferred orientation of the unused $2p$ orbital is normal to the triangular-planar shape (see 2.1(a)). Considering Pauli's law, only two electrons with an inverse spin can occupy an orbital. Hence, the formation of a hexagonal spaped carbon structure with a bond order of 1 is resulting. The $\pi 2p$ molecular orbitals form the valence band and the $\pi^* 2p$ molecular orbitals form the conduction band. These bands touch at six points in the unique band structure illustrated in 2.3(b). The 2-D energy states of
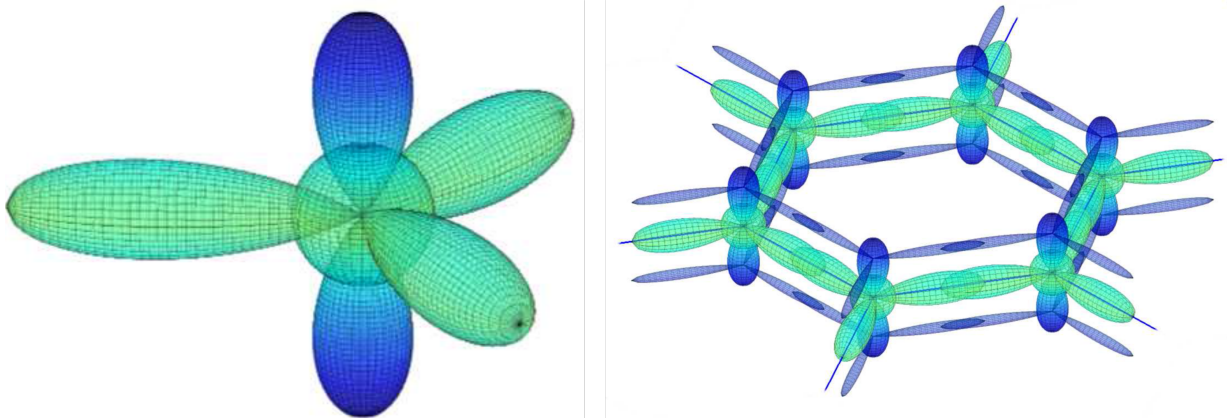
Figure 2.1: Left: sp^2-hybrid orbital; Right: Orbital of graphene honeycomb. Figure from [12]

the π-electrons were derived by Wallace [9]:

$$E_{2D}(k_x, k_y) = \pm\gamma_0 \left[1 + 4\cos\left(\frac{\sqrt{3}k_x a}{2}\right) \cos\left(\frac{k_y a}{2}\right) 4\cos^2\left(\frac{k_y a}{2}\right) \right]^{\frac{1}{2}} \tag{2.3}$$

γ_0 is the nearest-neighbor overlap integral, $a = 0.246nm$ is the in-plane lattice constant and k_x and k_y are the wave vectors. The positive solution represents the $\pi 2p$ band (valence band) and negative the $\pi^* 2p$ band (conduction band). [10] The unit cell consists of two carbon atoms, thus, in the first Brillouin zone we can focus on the points K and K' (see figure 2.3(c)). For electron transport we can limit the energy level and the band structure can be approximated by two antiparallel cones touching on their tops (see figure 2.3(d)). The pitch point of the cones is called Diracpoint at the energy level E_{Dirac} and, obviously, it's a good point to define it to $E_{Dirac} = 0eV$. Due to the lack of a bandgap, graphene is a zero band gap semimetal. Because of symmetry of the band structure, electrons and holes have the same properties in undoped, freestanding graphene. [11]
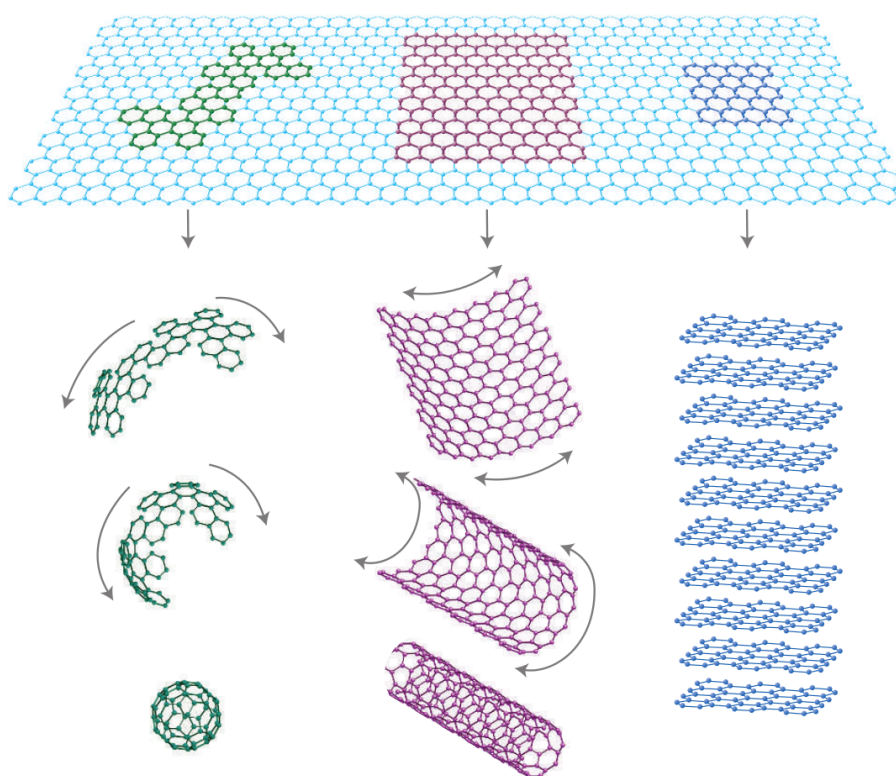
Figure 2.2: Green: Assembling of a fullerene. Purple: Assembling of a carbon nanotube. Blue: Assembling of graphite. Figure from [13].
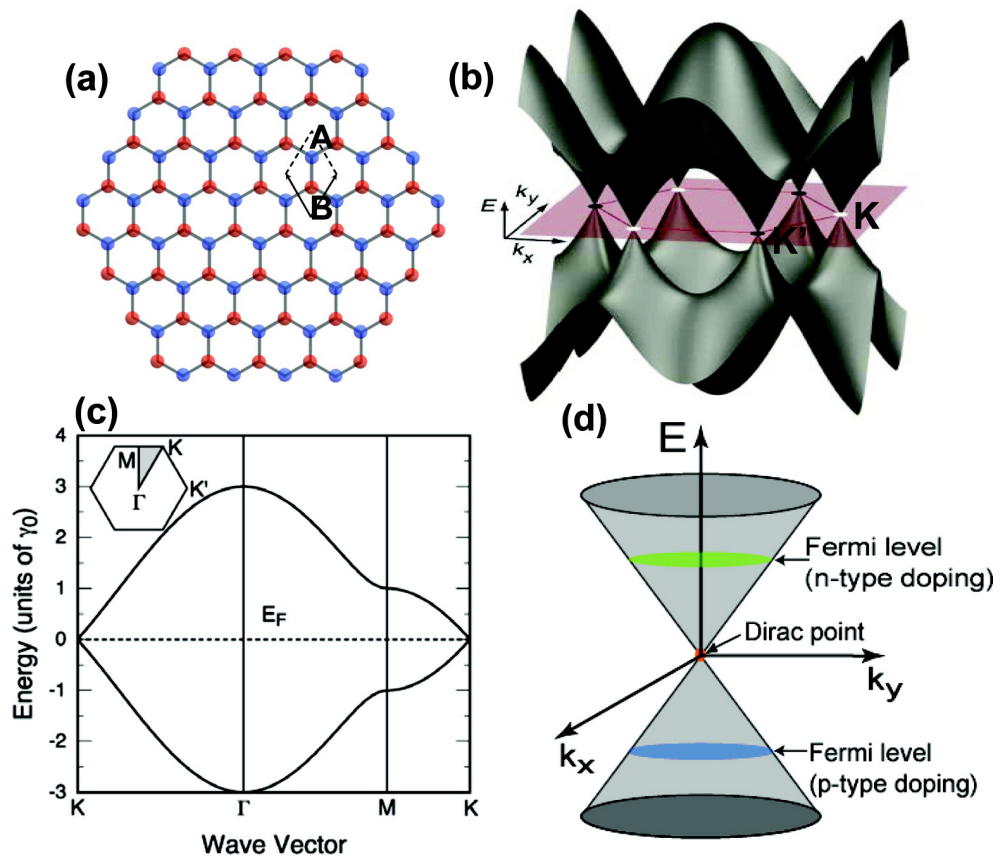
Figure 2.3: (a) Lattice of graphene and its unit cell. (b) Band structure of graphene. (c) Dispersion of the states of graphene. (d) Band structure for low energies. Figure from [11].

2.2 Charge Transfer Mechanism

2.2.1 Dirac Fermions in Graphene

The linear dispersion relation for small energy charge carriers can be described with

$$E(k) = \pm \hbar v_F k \tag{2.4}$$

where the positive equation describes the conduction and the negative the valence band. v_F is the Fermi velocity, which reaches values of approximately $10^6 cm^{-1}$ [14] and k stands for the wave vector. The band structure of graphene is reminiscent for that of light. The Hamiltonian of an electron in an energy range close to Dirac point can be expressed with

$$H_K = v_F \boldsymbol{\sigma} \cdot \mathbf{p} \tag{2.5}$$

where $\boldsymbol{\sigma}$ is a spinor like wave function and $\mathbf{p}$ is the momentum of the electron. $\boldsymbol{\sigma}$ describes a pseudospin corresponding to the hoping of the electron between the two atoms within the unit cell. Thus, electrons in graphene can be described as relativistic particles with its energy

$$E = \sqrt{m^2 c^4 + p^2 c^2} \tag{2.6}$$

where m represents the mass of the electron, c its velocity and p the particles momentum. As already mentioned, electrons and holes in graphene have linear dispersion. Comparing equation 2.4 with equation 2.6, one can immediately deduce that the rest mass is zero. Electrons behave in graphene like with zero restmass and, thus, act as massless Dirac fermions. Conductivity does not vanish for low charge carrier concentrations, much more it saturates to a value of $4e^2/h$. [15] [11] [16]

The Hall conductivity σ_{xy} in dependence of electron and hole concentration for graphene is illustrated in figure 2.4. The magnetic field is constant. Against expectations for quantum Hall effect (QHE), the plateau series is not $\sigma_{xy} = (4e^2/h)N$, where N is interger. Much more the first
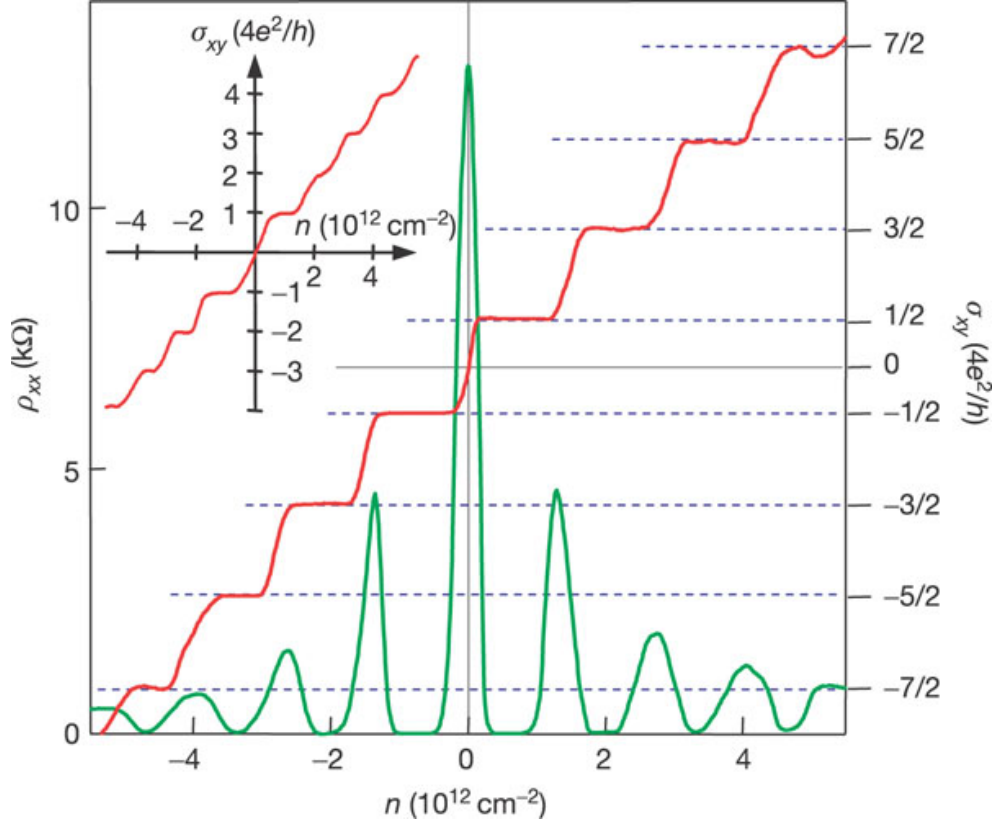
Figure 2.4: Quantum Hall Effect of single layer graphene sheet. The Hall conductivity follows the series $\sigma_{xy} = 4e^2/h)(N + 1/2)$. The inset shows the Hall conductivity of dual layer graphene. Figure from [14].

plateau occurs at half, $2e^2/h$ and the QHE follows the series $\sigma xy = (4e^2/h)(N + 1/2)$. For dual layer graphene the QHE returns to its normal behavior, a series starting with $4e^2/h$. This can be related to a finite mass near $n \approx 0$ and, thus, electrons can't be described as massless Dirac fermions anymore. Consequently, the half-integer QHE can be related to certain properties of massless Dirac fermions, in particular the existence of both electron-like and hole-like Landau states at zero energy.

$$E_N = \sqrt{2e\hbar v_F^2 B\left(N + \frac{1}{2} \pm \frac{1}{2}\right)} \tag{2.7}$$

where e represents the elementary charge, v_F the Fermi velocity, B the magnetic field and $\pm 1/2$ the pseudospin which occurs due to two sublattices of the carbon atoms in the unit cell. From equation 2.7 can be concluded that the lowest Landau Level with $N = 0$ appears at $E = 0$. Since the zero-energy Landau level is shared equally by electrons and holes, the first Hall plateau occurs at half the normal level at $\nu \pm 1/2$ and, thus, both correspond to the Landau level $N = 0$. [14]

2.2.2 Scattering Mechanisms

For graphene, we distinguish between three disorder which affect its mobility: **elastic scatterers** and **inelastic scatterers**. Elastic scatterers can be subdivided into

- **Long range scatterers**

- **Ripples**

and inelastic scatters result from **short range scatterers**. **Phonons** are known to be **short range scatterers**. According to [17], electron-phonon scattering has such a small impact, that charge mobilities of approximately $20,000 cm^2/Vs$ can be expected.

Long range scatterers like **charged impurity scattering** is caused by trapped charges on or near the graphene sheet [18][19][15]. Ripples are microscopic corrugations of a graphene sheet [6][20]. Local curvatures of graphene change the interatomic distances and angles between the carbon atoms [20]. If the characteristic honeycomb structure is altered, it's obviously that the unique electrical characteristic is changed. The curvature affects the nearest-neighbour hopping parameter and this leads directly into an occurence of vector and electrostatic potentials [20]. [11]

It was found that the conductivity can be modeled by superposition of a long range disorder term σ_L and a term σ_S, which is independent from the charge carrier concentration n and the temperature T. The long range term can be expressed as

$$\sigma_L = ne\mu \tag{2.8}$$

where e represents the elementary charge and μ the charge mobility. The resistivity of graphene can be described using the separation

$$\rho(V_G, T) = \rho_L(V_G) + \rho_S(T) \tag{2.9}$$

where ρ is the reciprocal of σ. **Long range scatterers**, expressed through ρ_L, are dependent on the applied gate voltage and independent from temperature below 300K. **Short range scatterers**, ρ_S, are dependent on temperature and show a rapid rise above 200K. As the resistivity becomes linear after subtraction of ρ_S in the vicinity of the dirac point, the characteristic can be approximated perfectly by a linear dependence on the gate voltage. [17]

The total charge carrier concentration, valid for electrons and holes, can be expressed by (2.10) [21].

$$n_{total} = \sqrt{n_0^2 + n(V_G)^2} \tag{2.10}$$

The residual carrier concentration n_0 should be zero for pristine graphene [21]. Charged impurities, hosted in the dielectric layer or its interface to the graphene, raise a finite charge carrier concentration. According to classical electromagnetism theory [22], the carrier concentration induced by the applied gate voltage can be expressed as

$$n(V_G) = \frac{C'V_G}{e} \tag{2.11}$$

C' represents the capacitance due to its spatial dimensions of the gFET device. In dependence of the thickness of the oxide layer, quantum effects, like quantum capacitance, have to be considered (see chapter 2.4).

The electrical resistance is direct proportional to the length and indirect proportional to the cross section of a conductor. Therefore, in our case of a conducting graphene channel, the resistance is proportional to the fraction W/L, where W describes the channel width and L its length. Consequently, the total device resistance is given by

$$R_{total} = R_S + \frac{1}{e\mu\frac{W}{L}\sqrt{n_0^2 + \left(\frac{C'}{e}V_G\right)^2}} \tag{2.12}$$

2.3 Contacts to Graphene

Graphene is contacted with with metals, like gold. These materials have different work functions, which causes charge transfer between them. Therefore, a dipole layer at the gold-graphene interface occurs. The dipole layer causes a doping of graphene at the area under the interface metal-graphene and into adjacent regions in the graphene channel [23]. Intentionally, one could expect that a negative doping of graphene would occur if the work function of graphene W_G is bigger than of metal W_M, i.e. $W_G > W_M$. Thus, it could be expected that no doping effects occur for $W_M = W_G$. This is where n-doping goes into d-doping, and, thus, called crossover point. The equilibrium distance between a graphene sheet and the metal surface is $d \approx 3.3\mathring{A}$. As illustrated in figure 2.5, for a distance of $3.3\mathring{A}$ an Fermi-level shift of $\Delta E_F \approx -0.55eV$ occurs for equal work functions. To vanish the doping effect a distance of $5\mathring{A}$ has to be attained. To achieve neutrality (no doping), a difference of work functions between metal and graphene of $0.9eV$ have to occur (see figure 2.5). Consequently, there is not only an electron transfer, it is also evidence for a chemical interaction between metal and graphene layer. Positive doping of graphene occurs in the case of $W_G > W_M$ and a dipole layer develops between the meta-graphene interface as illustrated in figure 2.6. Figure 2.7 shows the Fermi level change in dependence of the distance between metal and graphene sheet for different metalls. [24]

The charge carrier density becomes trapped in the graphene overlapping metal area. Thus, p-n or p-p' junctions occur, in dependence of the doping of the bulk graphene sheet. [25] Charge carriers have to be injected on the one metal-graphene interface and exhausted on the other interface. Therefore, carriers have to overcome both, the dipole barriers and the doped-undoped junctions.

2.4 Quantum Capacitance

Graphene can be modeled with a 2DEG (two-dimensional electron gas). Thus, due to accumulation of charge carriers, the energy level of occupied/unoccupied states are shifted. Therefore, in
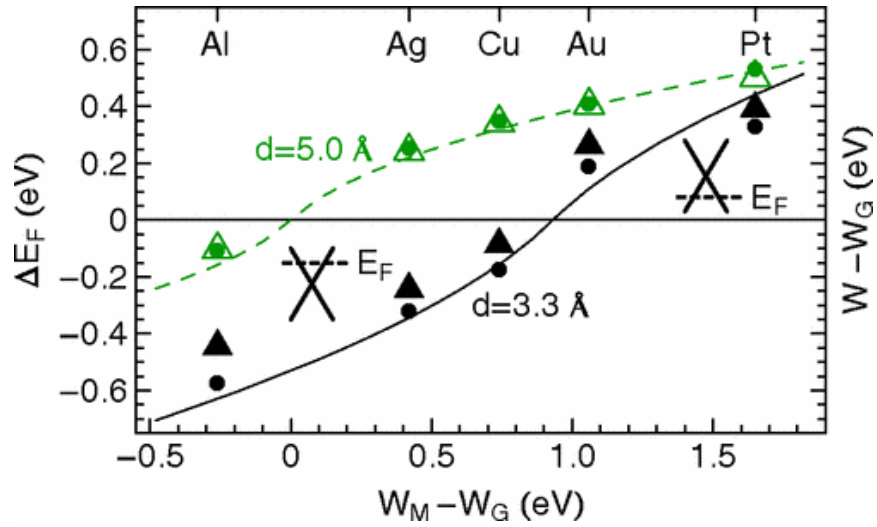
Figure 2.5: Calculated Fermi energy shift with respect to the conical point, ΔE_F (dots), and the change in the work function $W - W_G$ (triangles) as a function of $W_M - W_G$, the difference between the clean metal and graphene work functions. Functions are shown for distances between graphene sheet and metal $d \approx 3.3 \mathring{A}$ (black) and $d \approx 5 \mathring{A}$ (green). Figure from [24].
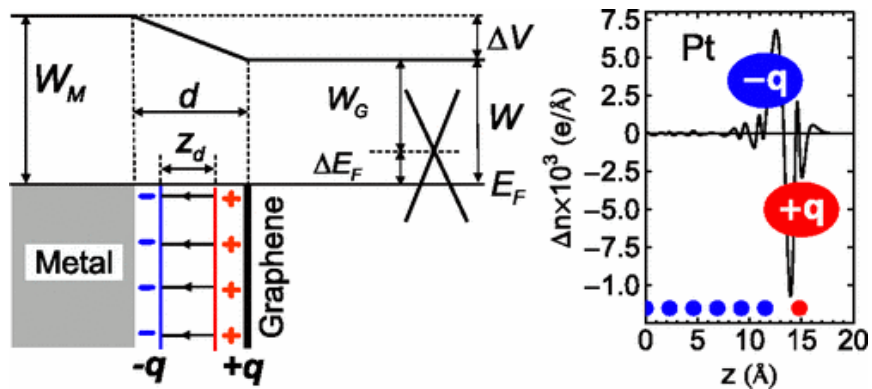
Figure 2.6: Left: Schematic illustration of bandstructure of the merging metal and graphene layer. Right: Difference in electron density due to formation of the Pt-graphene interface. Figure from [24].
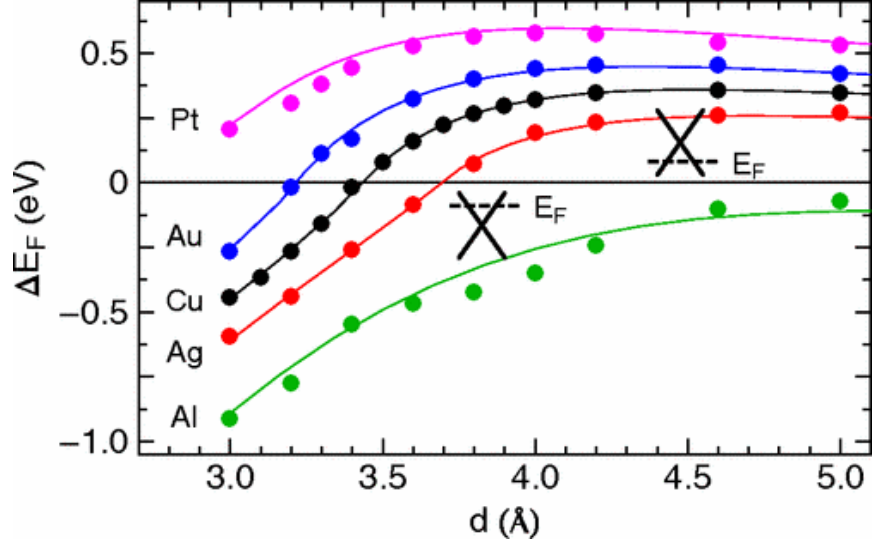
Figure 2.7: Fermi level shifts $\Delta E_F(d)$ as a function of the graphene-metal interface distance d. Figure from [24].

comparison to the voltage change, which can be explained by Gauß' law, another voltage change occurs. If the dimension of the oxide capacitor undergoes a certain thickness, these effect have to be taken into account. Finally, the system can be modeled with two capacitors in series: the common oxide layer capacity and the quantum capacity.

The total voltage which occurs on the graphene field effect transistor can then be modeled with

$$V_G = \frac{e}{C_{ox}}n + \frac{\hbar v_F \sqrt{\pi n}}{e} \tag{2.13}$$

where V_G represents the gate voltage, e the elementary charge, C_{ox} the oxide capacitance, n the total charge carrier density and v_F the Fermi velocity [21].

3 Immunoglobulins and Antigens
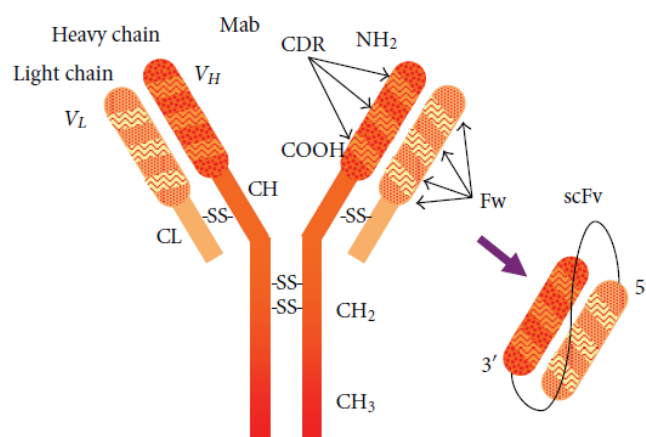
Figure 3.1: Chemical structure of Immunglobulin G. Pairs of heavy and light chains constitute the Y-pattern-shaped molecule. The antigen binding sites are formed by a light (V_L) and a heavy (V_H) chain. A pair of light and heavy chains form a scFv (single chain variable fragment). Figure from [26].

Antibodies and antigens form an antibody-antigen complex, if antibodies and antigens binding sites match with each others specifically. The strength between them depends on how close antibody and antigen do fit. It is called the affinity of binding between antibody and antigen. The most abundant antibodies in blood serum are Immunoglobulin G (IgG). The structure of IgGs has four polypeptide chains. The heavy chains (V_H) interact on the one end with antigens and at the other and form a branch to the light chaings (V_L). The V_H-chains are larger than the V_L-chains, thus the naming. Together, they form a Y-spaped molecule, as illustrated in figure 3.1. The specificity is achieved by the amino acid residues in the variable domains of the antibodies' (V_H)- and (V_L) chains. At the constant domains of the heavy and light chains the IgG can be cleaved with proteases. This results in a liberation of the basal fragment (Fc) and two single chain variable fragements (scFv, illustrated in the right of figure 3.1). These were used for
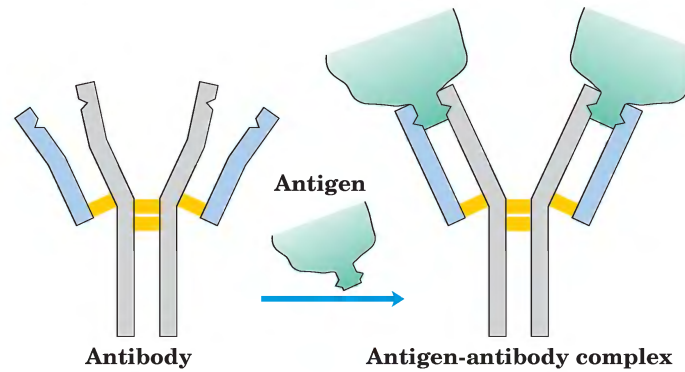
Figure 3.2: The antibody binds to the antigen (green). Figure from [27].
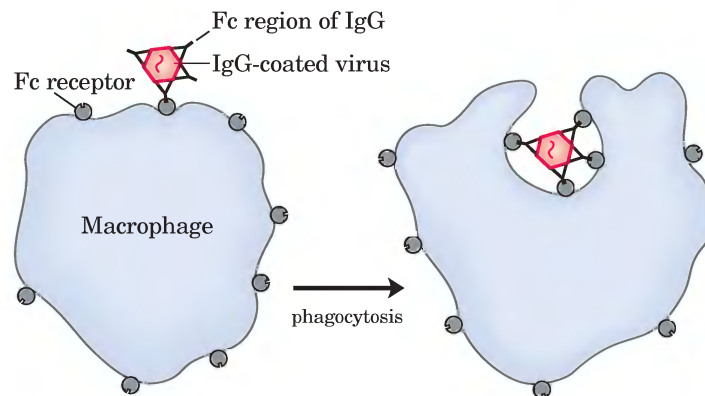
Figure 3.3: Phagocytosis of an antibody-bound virus by a macrophage. Figure from [27].

sensing, as explained later in chapter 5.

As already mentioned, the variable fragments of the IgG recognize the shape of antigens. Therefore, antibodies can differentiate between different viruses and bacteria. The binding interaction can thus be considered as a key-lock interaction, as illustrated in figure 3.2. Such a process serves as a tagging mechanism to protect the host from foreign cells and molecules. Tagged entities were ready for destruction, whereby the antigen itself does not harm the molecule. The destruction process is done by certain leukocytes as macrophages. These engulf the invading entity and start its destruction by binding its receptors to the Fc-part of the IgG, as illustrated in figure 3.3. The engulfment process is called phagocytosis. [27] [28]

4 Methods

4.1 Graphene Growth

The graphene exfoiliation method discovered by Novoselov and Geim [2] provides graphene with mobilities of up to $15,000cm^2/Vs$ at $300K$ and up to $60,000cm^2/Vs$ at $4K$, but the spatial dimensions are in μm-scale. For our purpose, we want to built graphene field effect transistor arrays with 52 devices per chip, which are reproducible in characteristic but also in fabrication, see chapters 5 and 6. Thus, we need large area graphene layers, which have to be fabricated in an easy and quick way. Therefore, low pressure chemical vapor deposition is used (LP-CVD) to yield graphene with high mobility.

Fabrication of single layer graphene was realized by low pressure chemical vapor deposition (LP-CVD). The LP-CVD setup existed of a MTI OTF-1200X furnace mounted on a MTI GSL-4Z gas supply system. For controlling the gas flow a Sevenstar D08-4E controller which was controlled remotely by a recipe software. The chamber was evacuated by a vacuum pump to reach a pressure of approximately 55mTorr. After heating up the chamber to $1010°$C, the $25\mu m$ copper foil was annealed for 60 minutes during a gas flow of 80sccm of hydrogen. Annealing of the copper film leads to big grain sizes, which is important to reduce scattering at the grain boundaries. The growth of graphene was realized with a gas flow of 10sccm methane for a growth time of 20 minutes. A schedule of the recipe is shown in Fig. 4.1.

The CVD growth of graphene on copper is a self limiting process [3], but a minimum growth time has to be satisfied to achieve a fully graphene covered film surface. As the copper foil thickness
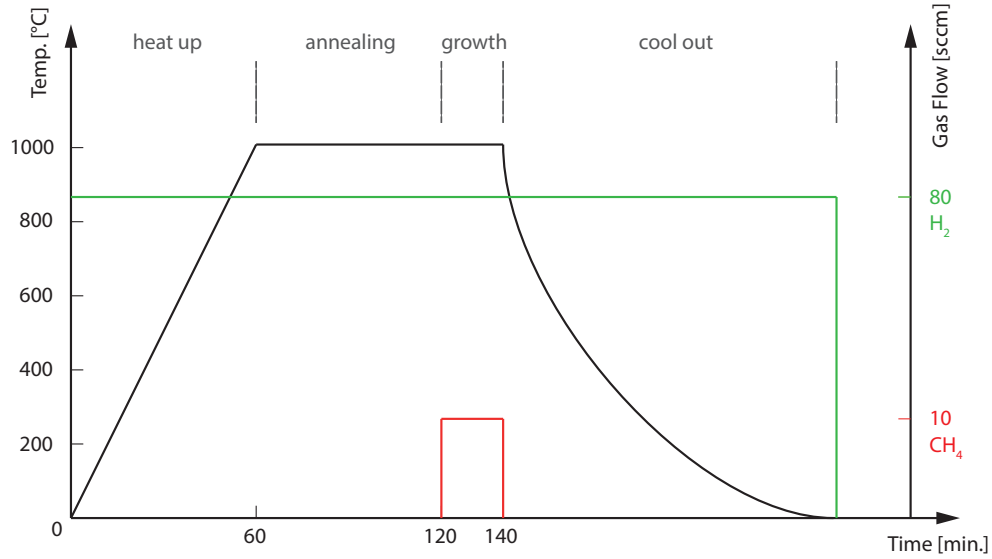
Figure 4.1: Graphene growth recipe using LP-CVD.

doesn't affect the thickness of graphene-layers, it was concluded that the growth is a surface-catalyzed process rather than a precipitation process as for nickel [3]. To ensure fully graphene coverage, and to check graphene quality, different characterization procedures like Raman spectroscopy were performed (see chapter 4.3).

During the CVD process copper is evaporating and condensing, so graphene grown on the top side of the copper foil is damaged due to condensing copper. Thus, the bottom side of the foil has to be used for further processing.

4.2 Device Fabrication

The chips which were used for contacting the graphene were fabricated by spincoating of a Si (100) p-doped wafer with a thermally oxidized 325nm SiO_2 layer or a 10nm ALD deposited Al_2O_3 layer with PMGI, as shown in Fig. 4.4(a), and positive photoresist 1813 (b). Continued by a backing step at 210°C for five minutes and 100°C for two minutes, respectively. The mask alignment and exposure was done with a Süss Microtec Mask Aligner MA6 3rd generation. After development (c), the contacts were evaporated by thermal evaporation of 5nm Cr and 40nm Au with a Kurt J. Lesker PVD 75 E-beam/Thermal Evaporator. Afterwards a lift of was performed
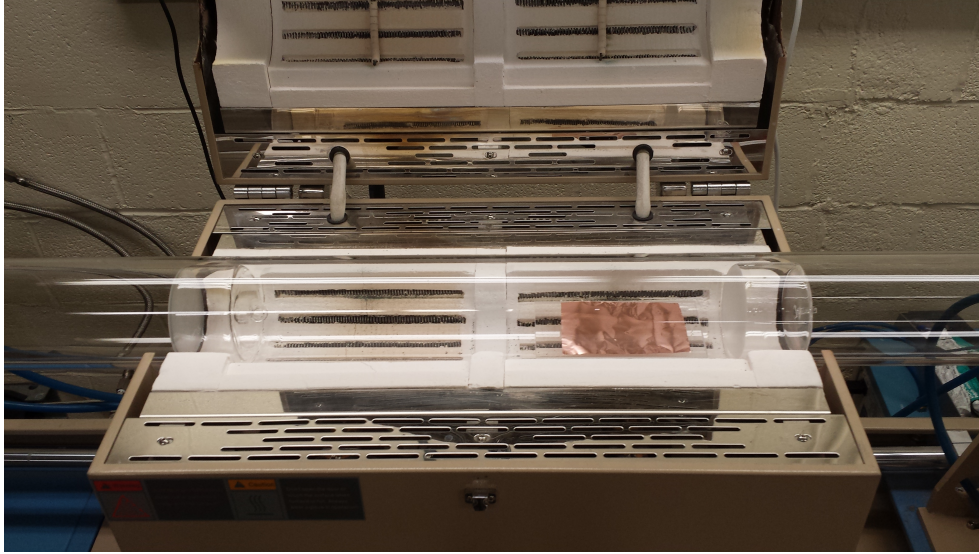
Figure 4.2: Evacuated chamber of the LP-CVD furnace. The copper foil lies on a crystal glass plate. The gas flow is from the left to the right.
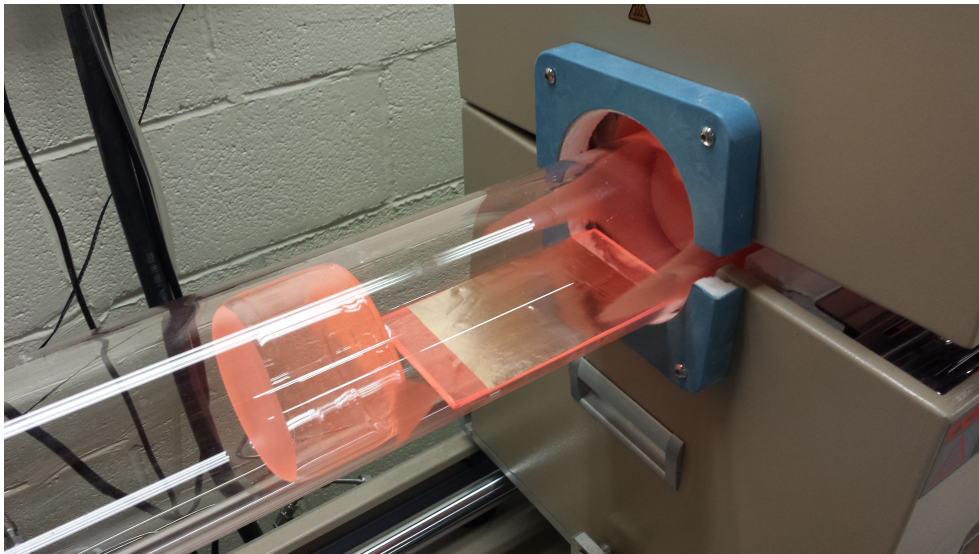
Figure 4.3: Evacuated chamber of the LP-CVD furnace in the cool down phase. The copper foil lies on a crystal glass plate. The gas flow is from the left to the right.

with a bath in 1165 for several hours. After cleaning the chips were ready for graphene transfer (d). The CVD grown graphene transfer was performed by the bubble transfer method, which is reported in [29]. Therefore the graphene on copper foil has to be cut, afterwards spincoated with PMMA-A4 and backed on the hotplate at 100°C for two minutes. The graphene-PMMA layer is separated from the copper foil by dipping it slowly and smoothly into a 0.05M bath of NaOH. The foil is connected to the ground potential of a 20V DC power supply, the NaOH solution
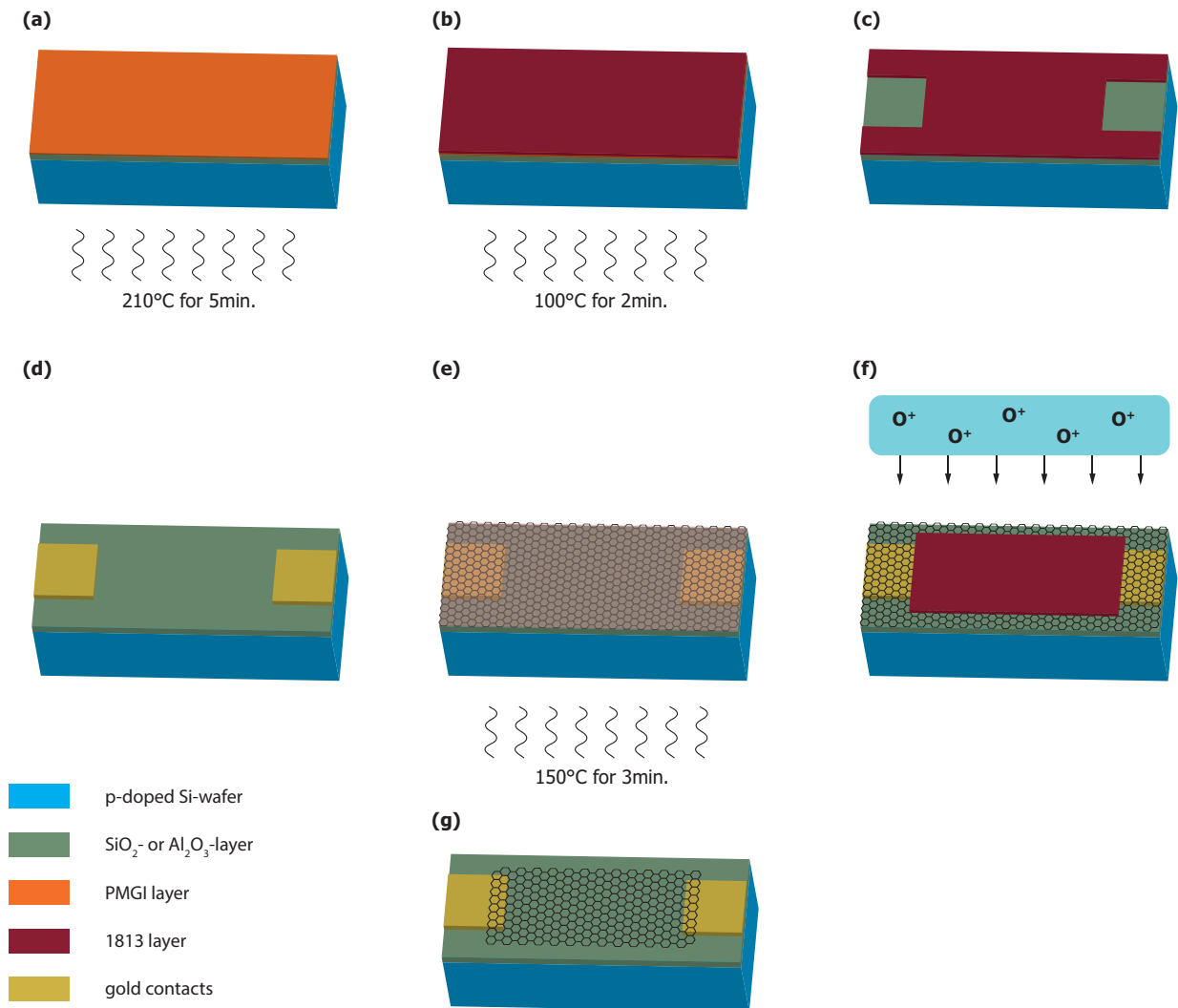
Figure 4.4: GFET chip fabrication process steps. (a) spin-coating with PMGI continued by a bake step by 210°C for 5 minutes, (b) spin-coating with 1813 continued by a bake step by 100°C for 2 minutes, (c) evaporating of the contacts using Cr and Au, (d) transfer of the graphene-PMMA-A4 layer on the top of the chip, (f) RIE etching with oxygen-plasma, (g) back gated, bottom contacted graphene field effect transistor

is connected with the positive potential. To remove the bubbles beneath the graphene-PMMA layer, it's transferred to a PMMA foil and afterwards transferred twice into a bath of deionized water. Finally the layer is transferred to the chip and has to be dried by ambient air for two hours. The process is illustrated in figure 4.5 schematically. The dried devices need to be baken on the hotplate at 150°C for three minutes, Fig. 4.4 (e), the PMMA-A4 layer is removed afterwards by a bath of acetone for five minutes, IPA spray and drying with nitrogen. The graphene is patterned again by photolithography with spinning of PMGI and 1813, baken at 120°C and
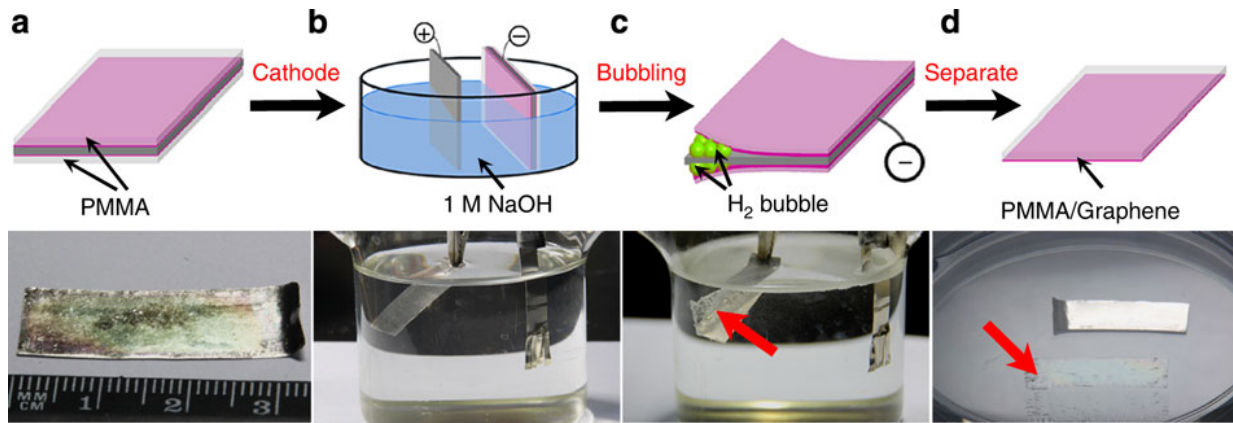
Figure 4.5: Concept of bubble transfer method. The H_2 bubbles provide the necessary force to detach the graphene-PMMA layer. Figure from [29].

100°C respectively. The graphene is etched by reactive ion etching with an oxygen plasma at 1.25 Torr pressure (f). Afterwards the PMGI and 1813 layer on the top of the graphene is removed by a bath chain of acetone and 1165, each for five minutes and again acetone for 30 minutes. To avoid acetone residues, an IPA spray was performed and afterwards dried by nitrogen (g). As already reported in [30], standard lithography processes cause residues of photoresists on the surface of the graphene layer. The contamination has a substantial impact on the transportation properties. To remove this contamination layer and oxygen and water residues, the chip was exposed to a reducing $H_2 - Ar$ atmosphere at an ambient temperature of 200°C. The annealing process was implemented with a one inch furnace with gas flows of 250sccm and 1000sccm for hydrogen and argon, respectively. To contact the back as the gate, the oxide layer was scratched and contacted with silver paste.

Finally, we built a matrix of 52 bottom-gated gFET devices separated to four blocks A-D, each 13 devices. Fig. 4.6 shows a quarter of the chip. For illustration purposes the photoresist was left to highlight the graphene covered areas. Having four gFET blocks has the advantage to measure four different concentrations of antigens in the sensing step. Further on, differences in the device characteristics can be evaluated.
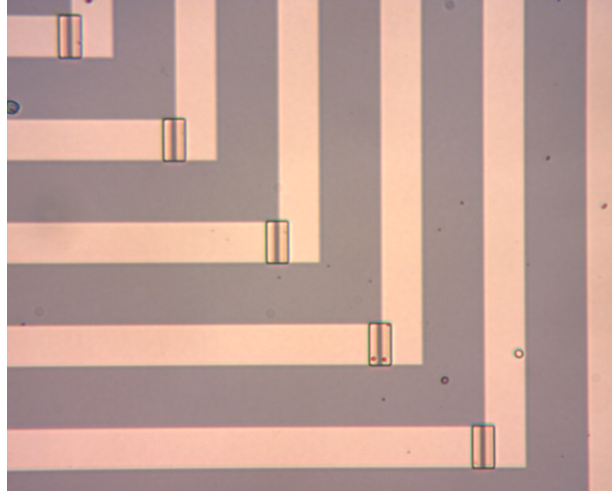
Figure 4.6: Surface of an Al_2O_3 chip after reactive ion etching. The squares illustrate the 1813 photoresist, which covers the transferred graphene layer.

4.3 Characterization

4.3.1 Graphene Coverage Evaluation

Figure 4.7(a) shows LP-CVD grown graphene (see 4.1) on copper foil with a growth time of ten minutes. As it can be clearly seen, the copper foil is partially covered with graphene crystals. To achieve better contrast, the foil was oxidized. For acceleration of the oxidation process, the foil was heated up to 180°C for one minute. Due to the coverage of the copper with the graphene crystals an oxidation of the underlying copper is not possible.

If you undergo a certain growth time, graphene won't cover the full surface of the copper foil [3]. To ensure full coverage a minimum growth time has to be satisfied, which turned out to be 20 minutes (see chapter 4.1).

4.3.2 Scanning Electron Microscopy Characterization

For determination of the number of grown graphene layers a SEM image was taken (figure 4.7(b)). Graphene was transferred to a SiO_2 wafer piece and SEM images were taken with a JEOL 7500F HRSEM. The green circle marks a scratch of the graphene layer, which happened during the transfer of graphene. This gives a nice contrast to the SiO_2-surface of the wafer and gives us a

Figure 4.7: (a) Optical microscope image of graphene crystals on copper after ten minutes growth time. Red: oxidized copper surface, not covered by graphene. Yellow: Graphene crystals. (b) SEM image of LP-CVD grown graphene layer on SiO$_2$. Green 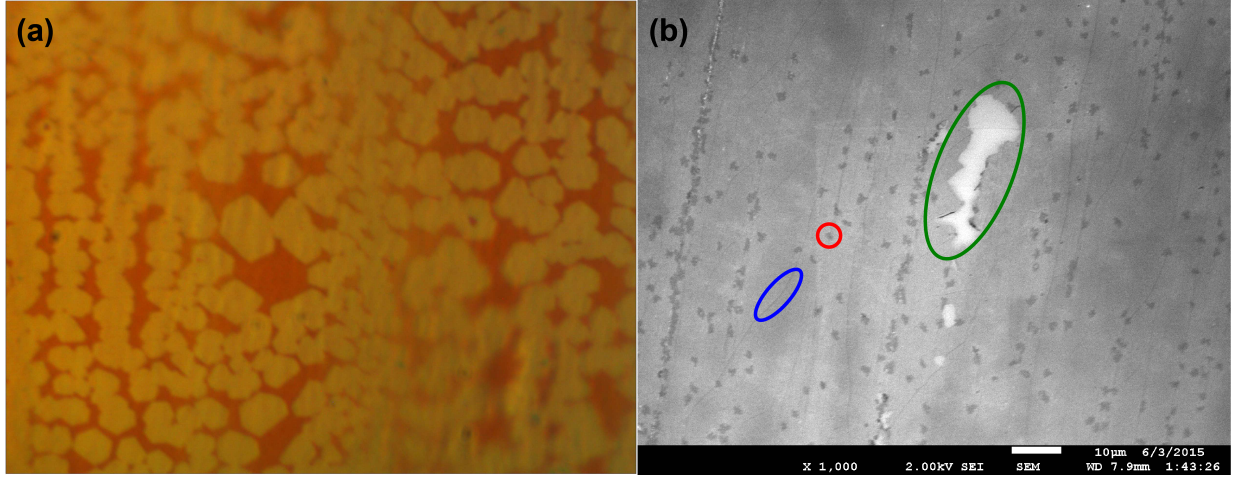circle: scratch of graphene layer due to mechanical strengths during transfer. Shows that the undamaged area is fully covered by graphene. Red circle: bilayer or multilayer graphene. Blue circle: wrinkle of graphene.

proof that the graphene film is continuous. The red mark shows a two-layer graphene flake and the blue a wrinkle of the graphene film, which happened during transfer.

4.3.3 Raman Spectroscopy Characterization of Graphene

Single layer graphene has two atoms in a unit cell (see chapter 2). We distinguish between **acoustic phonons** and **optical phonons**. Optical phonons do not vanish at the Γ-point of a dispersion relation. These have a frequency of $\omega_{optical} = ck$ and if a interaction between phonons and photons take place, optical phonons are involved. During such an interaction a photon will be absorbed, re-emitted at a different frequency and a phonon is emitted. Such a process is an inelastic scattering of a photon. [31]

At the Γ-point of the first Brillouin zone (inset of figure 2.3(c)), where the wave vector vanishes, optical phonons belong to the representation E_{2g} and B_{2g}. The E_{2g} mode consists of a longitudinal optical (LO) and a transverse optical (TO) mode with in-plane vibrations of the unit cell atoms in opposite directions. They are illustrated in figure 4.8(a) and (b), respectively. The atoms oscillate at approximately $1,582 cm^{-1}$. The optical phonons of the B_{2g} representation, ZO, oscillate in out-of-plane of the graphene layer, also in opposite directions as shown in (c). The

acoustic phonons ZA, illustrated in (f), do not contribute at the Γ-point but, different than the other acoustic branches longitudinal acoustic (LA) and transverse acoustic, as shown in figure 4.8(d) and (e), respectively, the dispersion follows a quadratic proportionality to the wave vector, i.e. $\omega \propto k^2$.[16]

Figure 4.10 shows the contributions to a Raman spectra of single layer graphene. At approximately $1,582cm^{-1}$ the so-called G-band occurs caused by first order Raman scattering with phonons wave vector $q \approx 0$. Beside the G-band occurring bands are associated with higher order Raman processes with $q \neq 0$. These can be be divided into *defect induced modes* were additional momentum is achieved by elastic scattering from defects and *excitation of two phonons*. In this case two phonons with opposite wave vectors q and -q are excited. Defect induced modes are the D-band at approximately $1,350cm^{-1}$, the D'-band at approximately $1,620cm^{-1}$ and the D" line at approximately $1,100cm^{-1}$.

To estimate the numbers of graphene layers, we are interested in the dependence of the Raman-spectra to strain, single- and multilayer or graphite and the behavior of each peak. The G-Band does not depend on the number of layers but much more on strain effects in the sp^2 system. If shifts occur, they can be caused by unintentional doping or strain. The 2D-band depends strongly on the number of layers. For single layer graphene it's located at approximately $2685cm^1$. For multiple layers the peak can be decomposed into sub-peaks and the Lorentzian 2D-peak of single layer graphene dissolves. The D- and D'-peaks are disorder induced and also can be decomposed into sub-peaks with dissolving Lorentzian. [16]

Figure 4.11(a) shows the Raman spectra excited with 514nm laser wavelength from [32] which was also used in our experiment. In figure 4.11(b) the Raman spectra of LP-CVD grown graphene is showed. We clearly see a G-band at$1583cm^{-1}$ which is in a good size ratio to the 2D-band. The grown graphene is of good quality which is proofed by the disappearance of the D-band.
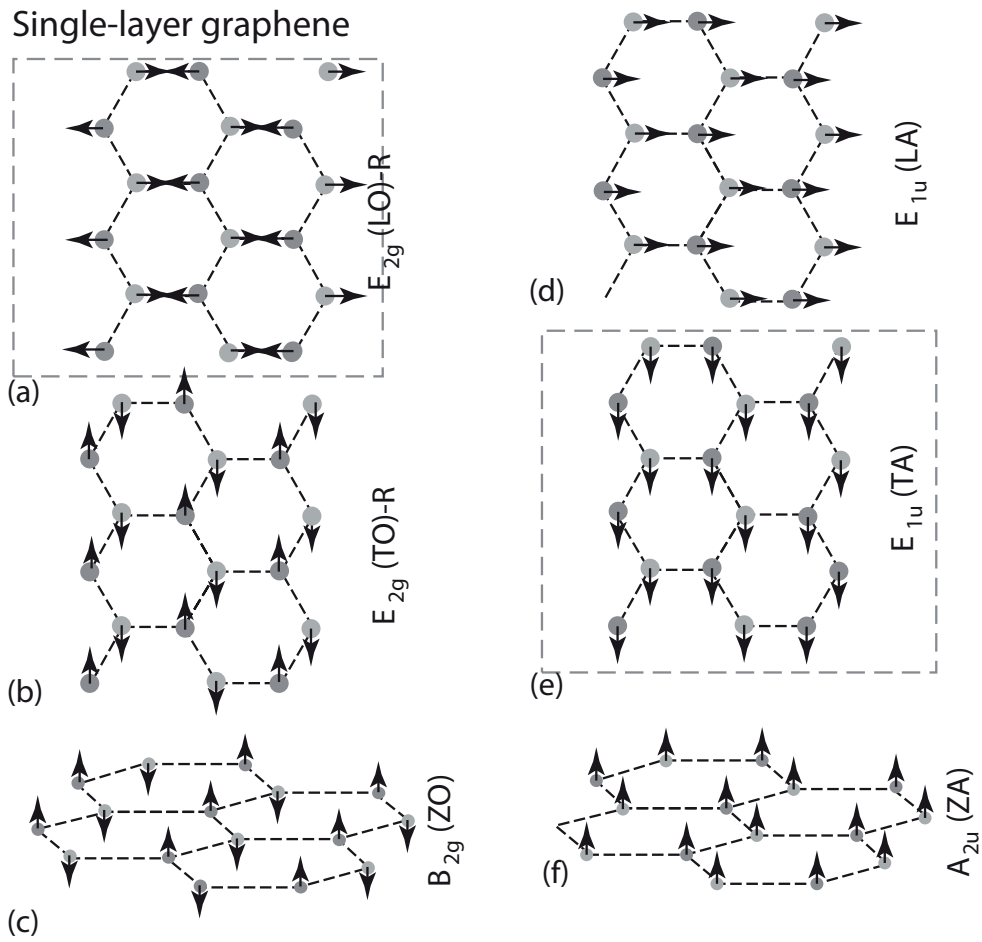
Figure 4.8: Eigenvectors of six normal modes at Γ-point of single layer graphene. Figure from [16].
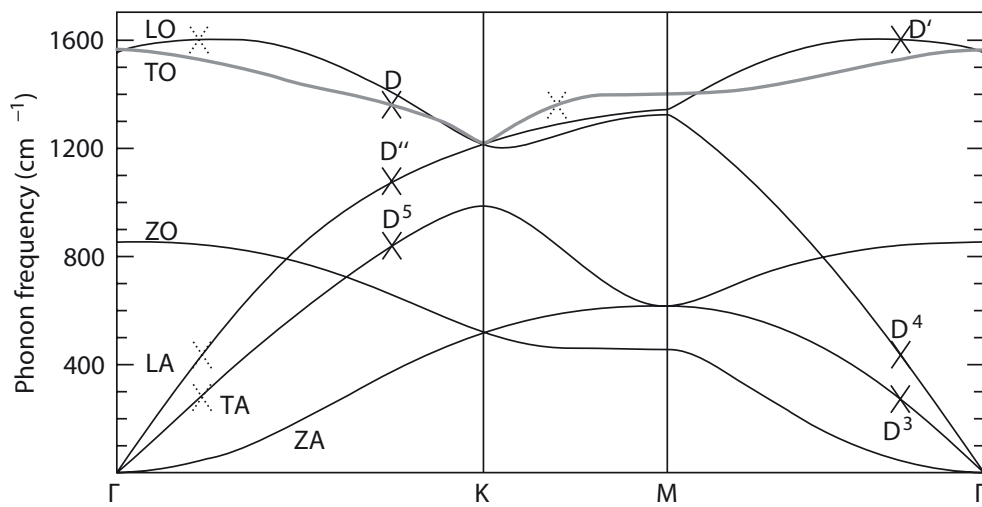
Figure 4.9: Phonon dispersion relation for single layer graphene sheets. The bold crosses indicate the responsible Raman modes. Figure from [16].
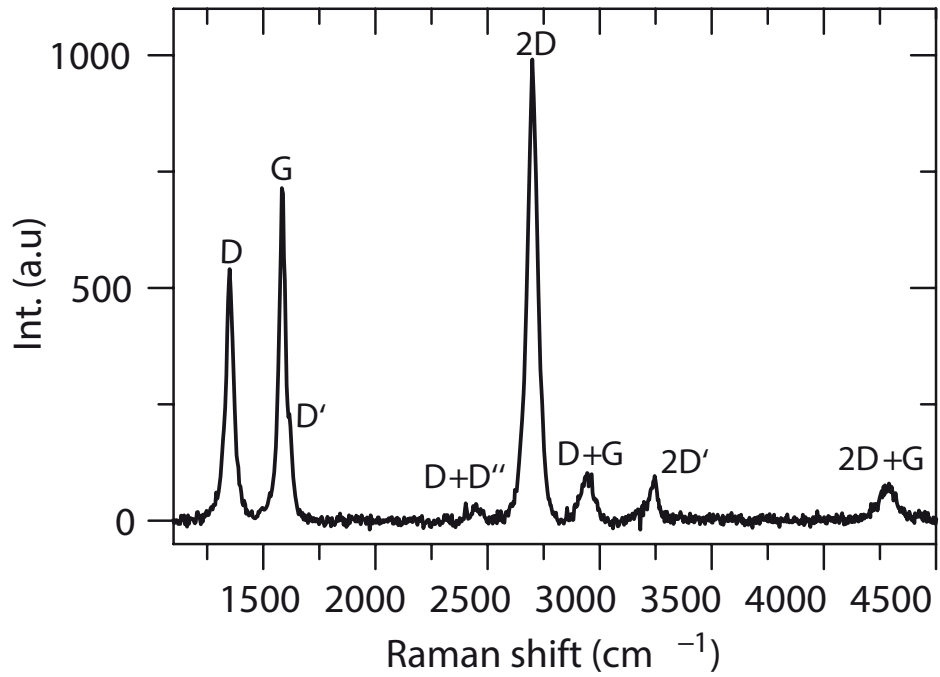
Figure 4.10: Contributions of optical and acoustic phonons to Raman spectra of single layer graphene. Figure from [16].
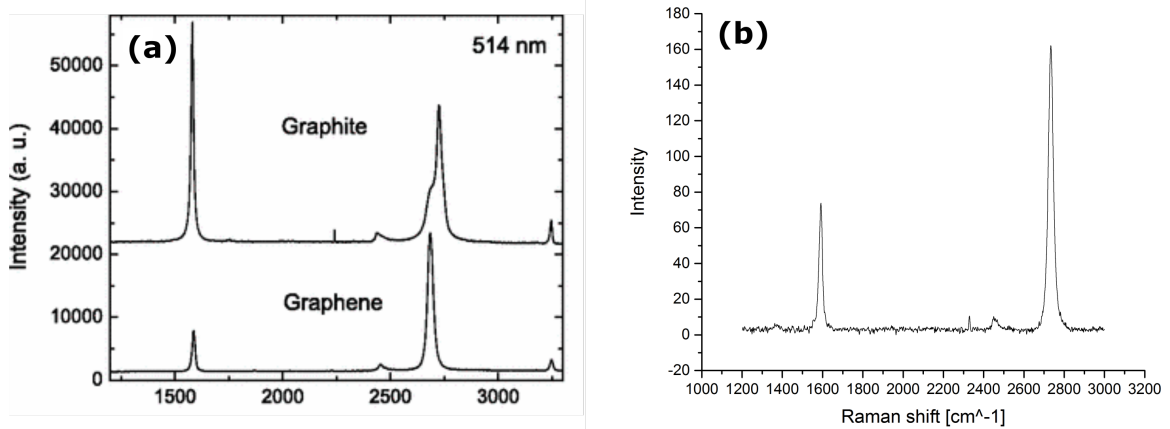
Figure 4.11: (a) Comparison of Raman spectra of graphite and graphene from [32]. (b) Raman spectra of LP-CVD grown graphene sample on copper.
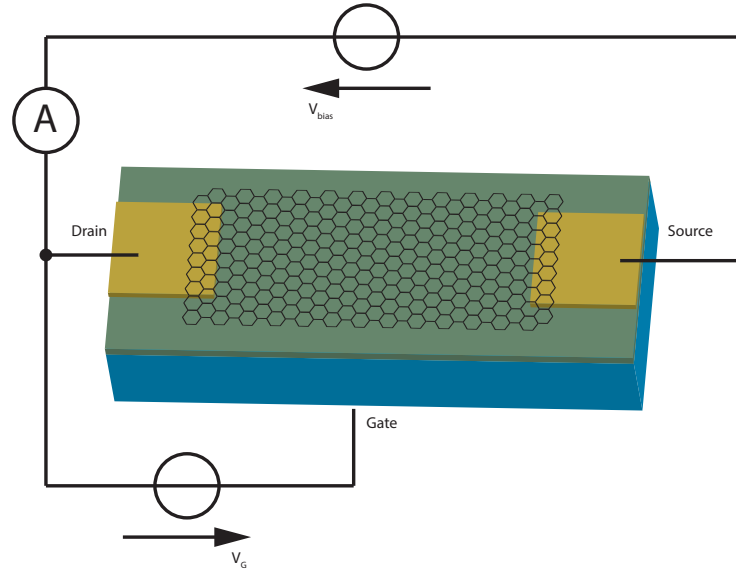
Figure 4.12: Setup for electrical characterization of gFET devices

4.3.4 Electrical Characterization of gFETs

Figure 4.12 shows the setup for electrical characterization of the gFET devices. A constant bias voltage of 0.1V was applied and its current was measured during sweeping the gate voltage from $-20V$ to $10V$ for SiO_2-devices and from $-1.5V$ to $1.5V$ for Al_2O_3-devices. The characteristics are shown in chapter 5 and chapter 6, respectively. Due to the shifts caused by the chemical functionalization steps the gate voltage sweep has to be increased to keep the electrical characterization window of interest (i.e. especially the Dirac point and its surrounding flanks) in the measured gate voltage sweep.

4.4 Atomic Layer Deposition

Instead of SiO_2 as the insulating oxide layer, another approach with 10nm Al_2O_3 (alumina) as oxide layer was performed. For deposition of alumina on a Si-wafer atomic layer deposition with trimethylaluminium (TMA, $Al(CH_3)_3$) as precursor was used. The process was run with a Cambridge Nanotech S200 ALD. First, the native, thermally grown SiO_2 layer has to be removed. This strip was realized with a HF buffer bath for five minutes. After cleaning, the wafer was heated up to $250°C$ in the chamber of the ALD. As illustrated in 4.13(A), the Si-surface has to

be passivated with hydroxyl (OH) groups. Then TMA is added to the chamber (B) and reacts under the creation of methane (CH_4) (C). After purging of the chamber with a nitrogen flow (C) water is pulsed into the chamber which reacts with the methyl groups to OH groups, again with the byproduct of methane (E-F). After a final purge step a layer of alumina is formed (G). [SOP for ALD, Singh Center for Nanotechnology]
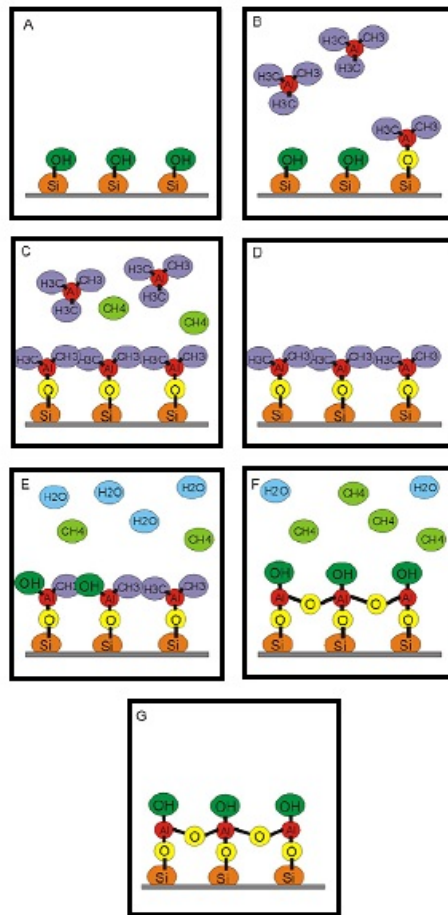

Figure 4.13: Chemical process steps of atomic layer deposition of Al_2O_3. Figure from Singh Center for Nanotechnology.

4.5 Immobilization of Proteins

Attachment of the Linker

For the attachment of the HER3 scFv-antibodies (single chain variable fragment) Pyrene-NHS ester (1-Pyrenebutyric acid N-hydroxysuccinimide ester, CAS-No. 114932-60-4) was used. The hexagonal shaped organic ring of the Pyrene-NHS ester, as shown in fig. 4.14, forms $\pi - \pi$ stacking interactions (see chapter 5.1.1) with the hexagonal honeycomb lattice of the graphene layer.

For the attachment of the pyrene-NHS ester the gFET-array chip has to be exposed to a 1.3M bath of pyrene-NHS ester in methanol. After an exposure time of one hour, the chip has to be cleaned by a one minute bath of methanol continued by a one minute bath of IPA. Finally, the chip has to be dried with nitorgen.

Immobilization of the scFv-Proteins

After the attachment of the pyrene-linker, the antibody-scFv has to be linked to the pyrene molecules. Therefore, on each quarter of the chip a drop of the HER3-antibodies has to be applied. To maintain a sufficient humidity to avoid evaporation of the antibody solution on the top of the graphene layer, the chips have to be put into a humid-chamber. The source of humidity is some boiled deionized water in a small dish inside the chamber. After one hour reaction time, the chip has to be cleaned in three baths of deionized water, each one minute and finally again carefully dried with nitrogen.

Blocker Attachment

To avoid binding of antigens with its amide groups (NH_2) to vacant pyrene-NHS ester groups (see figure 5.3(a) 1. left and chapter 5.1.2), a blocker is attached. The buffer consists of a 4mM solution of amino-ethanol in a PBS buffer solution. HCl has to be added until a pH of 8.5 is reached. To apply the buffer, the chips have to have a bath for 30 minutes in the buffer, similar
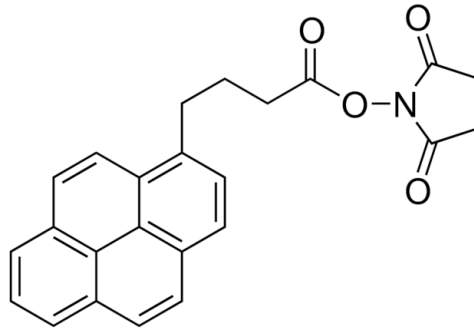
Figure 4.14: Chemical structure of 1-Pyrenebutyric acid N-hydroxysuccinimide ester ($C_{24}H_{19}NO_4$). ©Sigma Aldrich

to the application of the pyrene-linker. Again, the chip has to be cleaned with three baths of deionized water, each for a duration of one minute and drying with nitrogen.

HER3 Antigen Immobilization

For obtaining the calibration curve, we used different concentrations of antigens in buffer solution. The antigen concentration ranges from 3.1μg/ml to 0.31pg/ml and zero as reference.

- 3100ng/ml in buffer solution

- 310ng/ml in buffer solution

- 31ng/ml in buffer solution

- 3.1ng/ml in buffer solution

- 0.31ng/ml in buffer solution

- 0.031ng/ml in buffer solution

- 0.0031ng/ml in buffer solution

- 0.00031ng/ml in buffer solution

- 0ng/ml in buffer solution (pure buffer solution)

Buffer solution consists of a 0.1M sodium phosphate and 0.15M sodium chloride solution at a pH of 7.2.

5 SiO$_2$-gFET Devices for Sensing

Nanomaterials offer a new approach for electrical detection of chemical compounds or biological entities for two reasons. First, we have a size compatibility, as already explained in chapter 1 and illustrated in figure 1.1. The second reason is the fact that most biological processes involve electrostatic interactions and charge transfer [8]. These interactions enable electronic detection of biologicals merging with nanomaterials.

Graphene exposes its full volume to its environment (see chapter 2). Thus, every single atom of the material is accessible from its surrounding. Further, it shows very good electrical conduction, exhibiting metallic character and high mobility. Therefore, graphene is very accessible for doping. In [15] doping with potassium was demonstrated. The Dirac voltage of the devices were shifted to the negative scale, which is equivalent with negative charge carriers on the graphene. Since potassium has one electron in the valence band, it is in accordance with the expectations of negative doping. Detection of individual gas molecules adsorbed on graphene was demonstrated in [6]. Chemical doping with NH$_3$, CO, H$_2$O and NO$_2$ was performed and resulted in a shift of Dirac voltage to positive scale for NO$_2$ and H$_2$O, which corresponds to act as an acceptor dopant. NH$_3$ and CO showed donating character. Sensors have the task to detect certain molecules. Thus, some interface is needed which specifically docks onto the triggered chemical compound as soon as it comes in contact with it. Single-stranded DNA was used in [33] as an interface to make a gFET device specific for certain odors. After exposure the Dirac voltage of the device resulted in a shift into positive gate voltages. Building on this approach, [7] uses 4-carboxybenzenediazonium tetrafluoroborate as chemical linker following to a covalent sp^3 hybridization bond. Covalent bonds change the potential structure of graphene seriously and this results in a big reduction of

charge mobility.

To keep good device mobilities, in this approach we used 1-pyrenebutyric acid N-hydroxysuccinimide ester (pyrene-NHS ester, see figure 4.14) to bind HER3 scFv-fragments as a chemical receptor on graphene. The attachment to graphene happens by $\pi - \pi$ stacking interactions which results into much smaller influence in electronic quality. The scFv-fragments were specific to bind HER3 antigens. During the binding process between the IgG-scFv and the antigen, a charge transfer occurs (see chapter 3). If this electrostatic process is closer to the graphene surface, the influence to its electrical properties is expected to be higher. Thus, the basal fragment of the IgG was detached and only scFv-fragments were used.

5.1 Immobilization Procedure

5.1.1 $\pi - \pi$ Stacking Interaction

According to [34], a $\pi - \pi$ interaction can be represented as

$$E_{total} = E_{electrostatic} + E_{induction} + E_{dispersion} + E_{repulsion} \qquad (5.1)$$

The major contributions to the interaction energy come from the electrostatic and van der Waals components. van der Waals interactions are direct proportional to the overlap area of the π-orbitals and can contribute an appreciable contribution to the magnitude of the $\pi - \pi$ interaction. Due to the proportionality of the area of the π-orbital overlap, van der Waals forces can't be responsible for the geometry of $\pi - \pi$ stacking interactions. In this case, the overlap would be maximized and a cofacial arrangement would be observed. Experiments in [34] yielded in a non-distortion of each others molecular orbitals of the interacting π-systems. Thus, the molecular orbitals remain unchanged and the systems interaction can be described using two facing sp^2-hybridization orbitals. As illustrated in figure 5.1, the negatively charged clouds of the molecules non-participant p-orbital, which is orthogonal to the preferred direction of the sp^2-hybrid orbitals as shown in fig. 2.1, are cofacial and, therefore, repulsion effects occur.

Figure 5.1: (a) Negatively charged clouds of two 2p orbitals face and repulsion forces occur; Interaction between two idealized π-atoms for three possible geometries, (b) face-to-face: $\pi - \pi$ repulsion dominates, (c) T-shape: $\pi - \sigma$ attraction dominates, (d) offset: $\pi - \sigma$ attraction dominates. Figure adopted from [34].
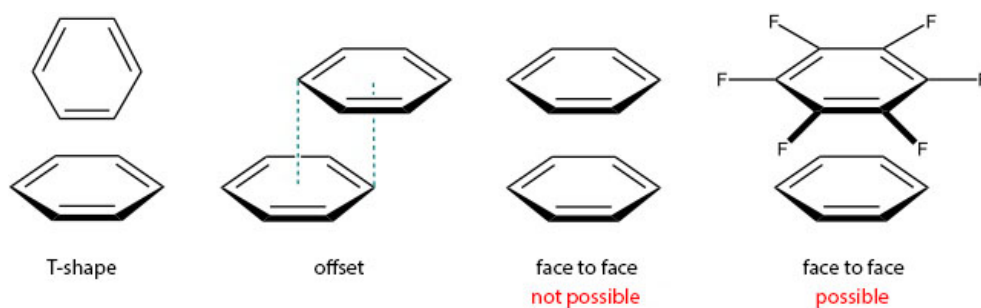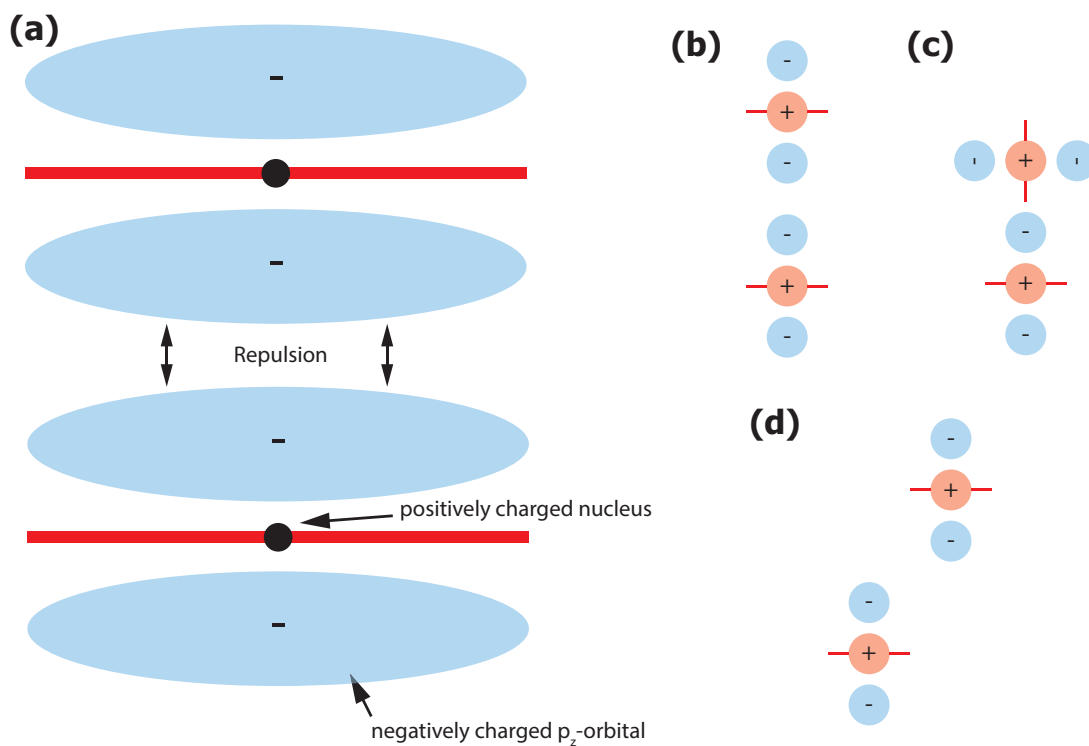

Figure 5.2: $\pi - \pi$ stacking interaction geometries. Figure adopted from [35].

Finally, three general geometries have to be considered:

- $\pi - \pi$ repulsion terms disfavor the face to face interaction

- $\pi - \sigma$ attraction terms dominate the T-shape interaction

- $\pi - \sigma$ attraction terms dominate the offset interaction

So far, only unpolarized atoms were considered. For the case of polarized system atoms, also cofacial attractive $\pi - \pi$ interactions are possible [34]. In figure 5.2 the skeletal formula and its spatial orientation of the molecules are illustrated. In the case of benzene and hexaflourobenzene a cofacial orientation is possible due to its compensating polarization.

5.1.2 Protein Attachment Mechanism

As explained in chapter 2, graphene has a honeycomb lattice built of carbon atoms. The hexagonal shape enables $\pi - \pi$ stacking interaction with structures, assembled with benzene rings. For this approach pyrene ($C_{16}H_{10}$) was chosen to provide the required binding interface to the pristine graphene surface. Attached to pyrene, you find a N-hydroxysuccinimide ester group, illustrated in figure 5.3 step 1. The antibody fragments (scFv) have an amide group (NH_2), which attacks the carbonyl group (step 2). In solution the carbonyl group is protonated and the carbonyl group becomes available to be attached by amine. The electronegativity of oxygen is bigger than of nitrogren, so its affinity of binding an atom is higher, thus one electron on the amine group is detached and bonded to the NHS group (step 3). Finally, the scFv-protein is attached to pyrene and additionally we have the NHS-group (step 4).

During the binding process, methods outlined in chapter 4.5, there may remain unfunctionalized pyrene-NHS ester groups. To avoid binding of these groups with antigens during the latter antigen attachment process, a block was attached (method explained in chapter 4.5). The block consists of a ethanol-amine group. Analogous to the binding process of the protein-fragment, the blocks amine group reacts with the carbonyl group. After binding an ethanolamine molecule to a pyrene-NHS, it's passivated because the block has a hydroxyl group attached to the open end.

Figure 5.4 shows an illustration of the via pyrene-NHS ester to graphene attached antibody fragment.

5.2 SiO$_2$-Graphene Field Effect Transistors

Figure 5.5 shows the electrical characteristic of a gFET device array. Hole mobilities of up to $5,000 cm^2/Vs$ were achieved with a maximum device frequency between $1,500$ and $2,500 cm^2/Vs$. Mobilities were calculating by fitting the conductivity model as explained in chapter 2.2. As already mentioned, due to the symmetry of the band structure of graphene (see figure 2.3), electrons and holes have the same mobility. However, the junction contact-graphene develops a pn-junction and, therefore, electrons have to overcome a potential (see chapter 2.3). This effect can be seen in the smaller slope for positive gate voltages in comparison to the negatives. Thus, for calculation of the mobility, the electronic response for negative Dirac voltages was fitted and its parameters calculated. It expresses the hole mobility but because of the symmetry in bandstructure can also be treated as the electron mobility. Devices mainly show a Dirac point voltage of approximately $-4V$. This means that a voltage of $-4V$ has to be applied to reach the Dirac point in the band structure (see figure 2.3(d)). Dirac point represents a charge neutral graphene layer and in this certain case means an excess of negative charges and, therefore, a lowering of the occupied states. This is in agreement with [15].

For positive gate voltages, electrons are attracted due to the developed of an electrostatic field between the p-doped silicon bulk-silicon oxide interface. As explained in chapter 2, the attraction of electrons to the graphene layer corresponds to an n-doping and further, to a positive shift of the Fermi energy level (see figure 2.3). The deployment of a negative gate voltage causes an inverse electrostatic field in comparison to case of a positive voltage. This leads to an attraction of positively charges holes to the graphene layer and a negative shift of the Fermi energy level. Considering the negative Dirac point voltages of the devices in figure 5.5 and 5.6(b), an initial doping with an electron donator can be concluded. As the devices of the array show similar device-to-device characteristic, they can be considered as a sensing electronic device. This approach is
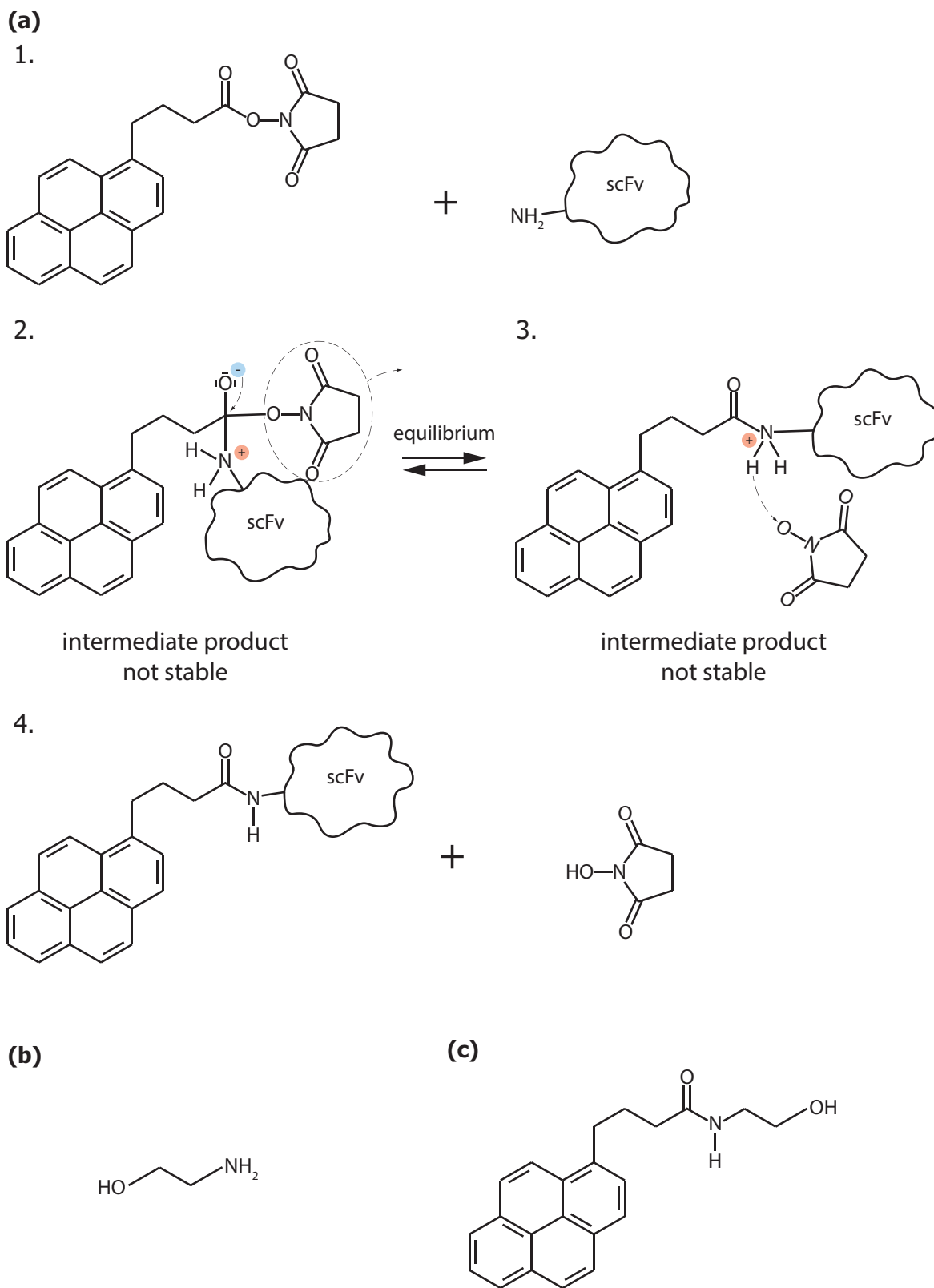
Figure 5.3: (a) Attachment mechanism of pyrene, (b) Block structure, (c) With block passivated pyre-NHS ester linker.
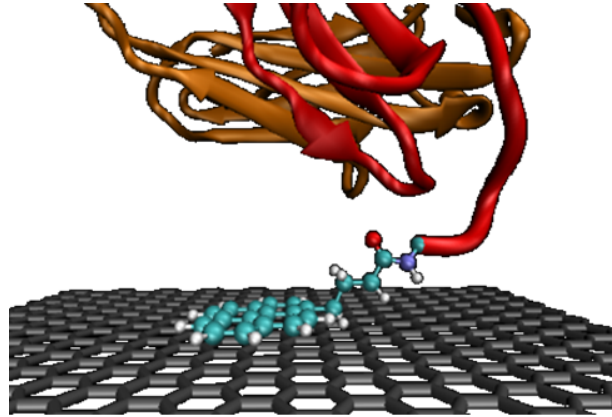
Figure 5.4: scFv-antibody attached with pyrene-NHS ester. The final chemical structure as shown in figure 5.3(a)4 is illustrated with Visual Molecular Dynamics. Figure provided by Madeline Diaz-Serrano.

Figure 5.5: IV-characteristics of a gFET-array based on a 325nm SiO_2 dielectric layer. The devices show very similar device-to-device characteristic.

discussed in the following chapter.

5.3 SiO_2-gFET Sensing

To draw conclusions about concentration levels of HER3 antigens in the applied buffer solution the electronic response was evaluated after each functionalization step. The characteristic was conducted after implementation of the steps

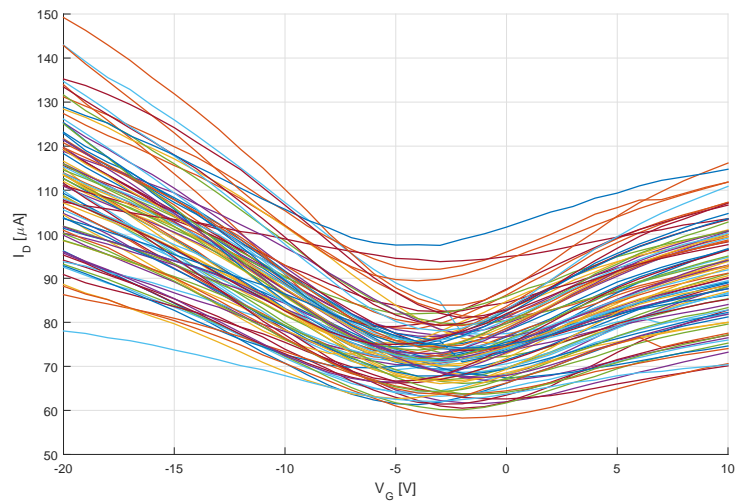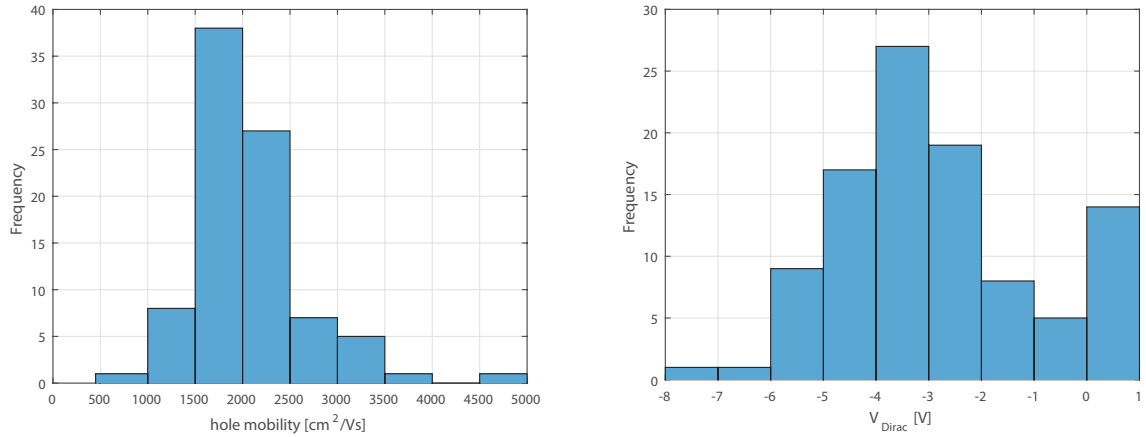- pristine graphene device after annealing process

Figure 5.6: IV-characteristics of a gFET-array based on a 325nm SiO$_2$ dielectric layer. The devices show very similar device-to-device characteristic.

- attachment of the pyrene-NHS ester

- attachment of the scFv antibody fragments

- attachment of the block

- exposure to HER3 antigens

Details are explained in chapters 4.2, 4.3.4 and 4.5. The gFET devices show an decrease of charge mobility after each functionalization step, which is in accordance with previous studies [15][30]. After annealing the pristine graphene device, they have mobilities of approximately 1,500±300Vscm^{-1}. After attachment of the HER3 antibodies a hole mobility of 600±200Vscm^{-1} remains. The hole mobilities after each functionalization step is illustrated in figure 5.7. Measuring the electrical characteristic after each characterization step resulted in a Dirac voltage shift to the positive scale, as shown in figure 5.8. Hysteresis effects between measurements were reduced with an annealing step as explained in chapter 4.2 according to knowledge from [30]. To consider the hysteresis shift, measurement of pristine devices for comparison was conducted. To ascertain a trend of characteristics, the electronic response of gFET arrays of 104 devices per chip, divided into four blocks A-D with similar device to device characteristic, was evaluated. Dirac voltages of the gFET-array are illustrated in figure 5.8. Considering the hysteresis shift we finally receive a calibration curve as illustrated in figure 5.9. There is a strong dependence in the Dirac voltage
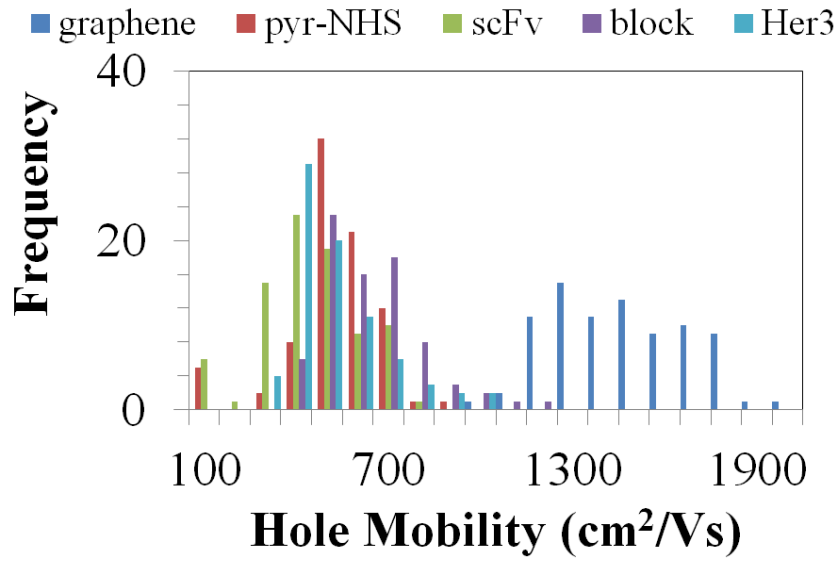
Figure 5.7: Hole mobilities in dependence of functionalization step. Data analyzed by Madeline Diaz-Serrano.

shift to the concentration of the HER3 antigens. To evaluate an optionally present buffer effect on the voltage shift, control experiments with pure buffer have been done (green line).
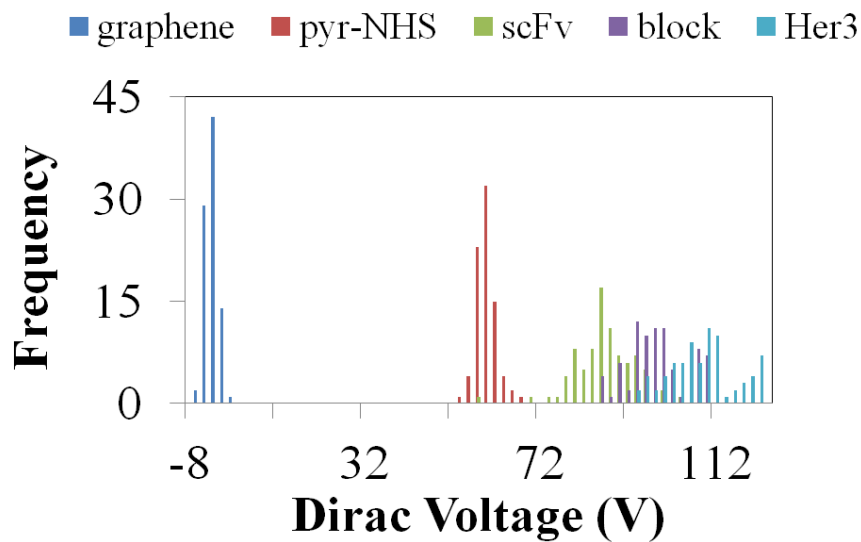
Figure 5.8: Dirac voltage shift in dependence of functionalization step. Data analyzed by Madeline Diaz-Serrano.
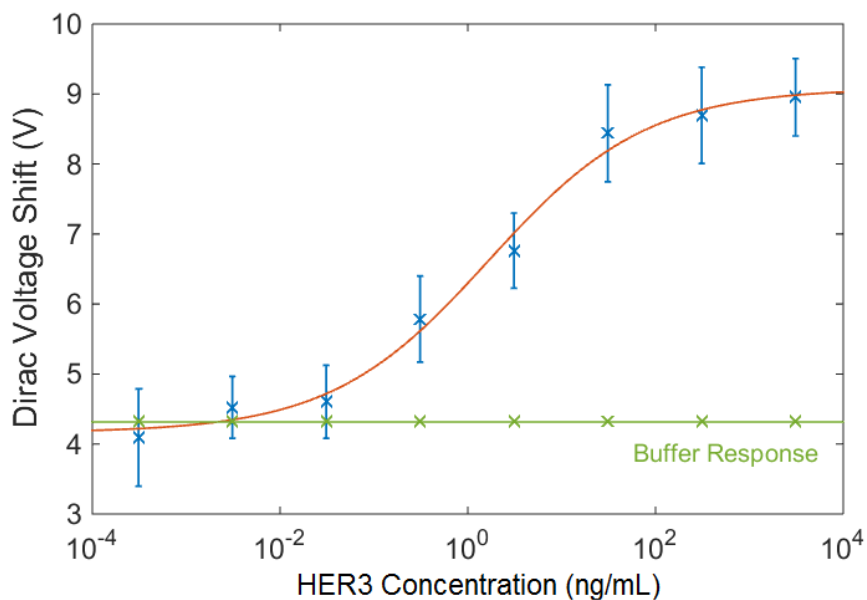

Figure 5.9: Langmuir-Hill fit of Dirac voltage shift in dependence of HER3 antigen concentration. Data analyzed by Madeline Diaz-Serrano.

6 Al$_2$O$_3$-gFET Devices for Sensing

Graphene field effect transistors based on SiO$_2$ devices have some issues, like high gate voltages, their big hysteresis and low time period of stability, which have big disadvantages for sensing accuracy. To overcome these issues, an approach with Al$_2$O$_3$ as dielectric layer has been started. Instead of the 325nm layer of SiO$_2$ a ALD deposited 10nm layer of alumina was used. The higher dielectric constant of $\epsilon_r \approx 9$ has an impact to the polarization of the dielectric layer, thus, less voltage is necessary to get the full characteristic.

6.1 Al$_2$O$_3$-Graphene Field Effect Transistors

Devices with high similarity in device-to-device characteristic were fabricated. Figure 6.1 shows the IV-characteristic of the Al$_2$O$_3$ based gFETs. The overall capacities of the devices devices did increase significantly. On the one hand the reduced thickness of the dielectric layer and its bigger dielectric constant did increase the oxide capacities, on the other hand quantum capacitance effects, as explained in chapter 2.4, have to be taken into account. Following from this, much smaller voltages have to be applied to the gate for attracting the same amount of charges to the interface. Hole mobilities up to $1,800cm^2/Vs$ were achieved. This might occur small in comparison to chapter 5.2 but it has to be considered that arrays of Al$_2$O$_3$-devices had a significant higher yield than SiO$_2$-devices in average. Dirac voltages of approximately $-0.25V$ did occur with highest frequency. In comparison with SiO$_2$-devices, the Al$_2$O$_3$-devices are more steady in time. The latter showed even after eight weeks good electronic response. As illustrated in figure 6.3, gFETs with a stable Dirac-point are realizable. The device was measured three
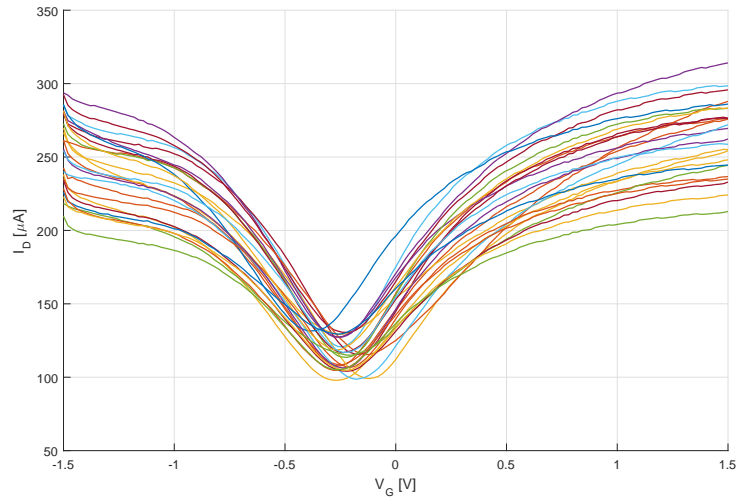
Figure 6.1: IV-characteristics of a gFET-array based on a 10nm Al_2O_3 dielectric layer. The devices show very similar device-to-device characteristic.

times consecutively, and no drift of the Dirac-point is observeable. For proper sensing, similar device-to-device characteristic, stable dirac points over time and a small hysteresis for consecutive measurements are important.

Further, the electron charge carrier disfavor-effect was not as distinct than in comparison with SiO_2-devices.

Figure 6.2: Histogram of hole mobilities and Dirac voltages of a gFET-array based on a Al_2O_3 dielectric layer.

Figure 6.3: IV-characteristics of a gFET, measured consecutively. The Dirac-points don't show a drift to higher gate voltages.

7 Conclusions

Arrays with 104 SiO$_2$-based graphene field effect devices with similar device-to-device characteristic have been demonstrated. Devic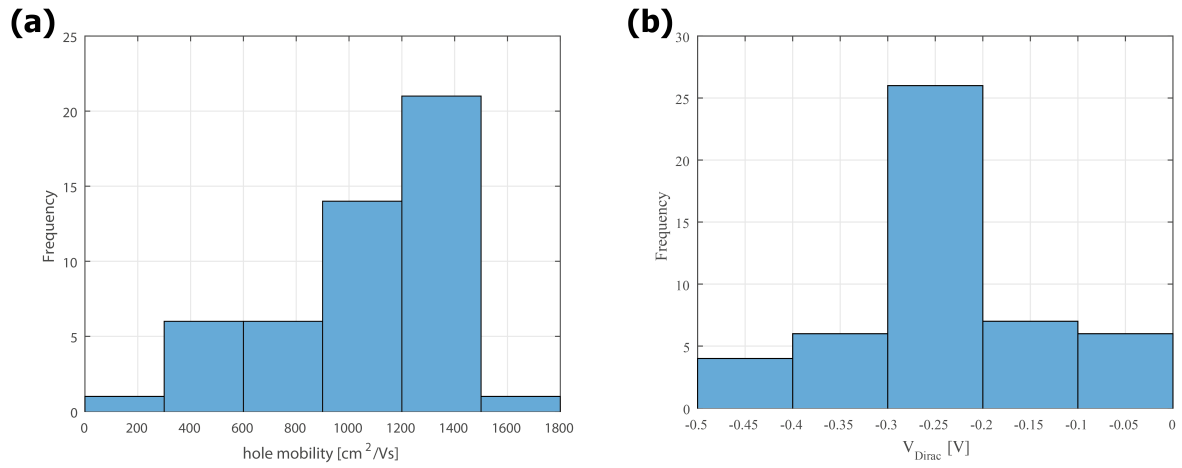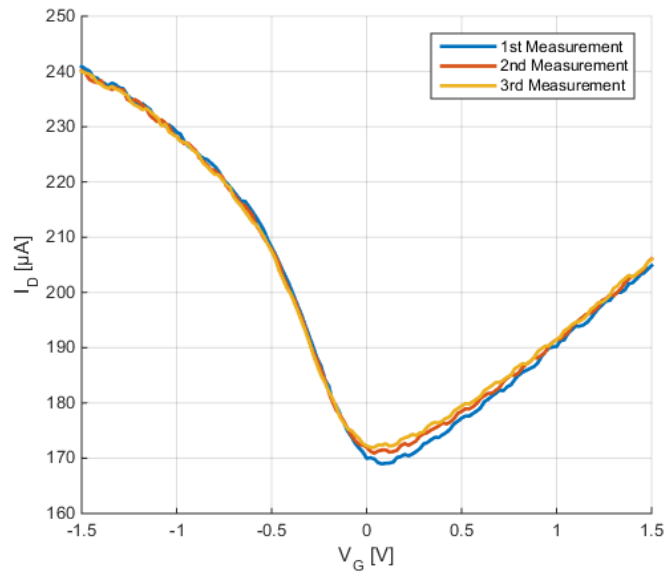es had an oxide layer thickness of 325nm, a channel length of $10\mu m$ and a width of $100\mu m$. Arrays with 54 devices have been demonstrated for 10nm Al$_2$O$_3$ oxide thickness and identical channel geometry. Graphene is an excellent candidate for sensing applications because every single atom does interact with its environment. Standard lithography processes were used for device fabrication and patterning. During these processes used polymers leave residues on the graphenes layer surface.

The functionalization process binds the aromatic ring shaped structure of pyrene-NHS ester with $\pi - \pi$ stacking onto the surface of graphene. The NHS-ester group interacts with the antibody-structure. To achieve higher impact of the charge transfer, which occurs due to binding antigens to the heavy (V$_H$) and light (V$_L$) chains of the Immunoglobulin G (IgG), only the single chain variable fragments (scFv) were used. The pyrene-scFv complex acts as interface for antigen detection. The sensor gets its specificity by binding scFv antibodies which himself only interacts with matching antigens. Since most IgG scFv have amide groups in their chemical structure, this approach can be generalized. After binding of antibodies, a voltage shift for the Dirac voltage did occur. As this shift has been into positive direction, it can be concluded that the binding led to a doping with positive charge carriers. The voltage shift has been detectable for target antigen concentrations of as small as pg/ml.

Device stability over time and device-to-device characteristic are a challenging issue. Further on, the high gate voltages which have to be applied for SiO$_2$ are an issue for point-of-care sensing

devices. Therefore, an approach with Al_2O_3 has been developed. High device yield and very good device-to-device characteristic were achieved. Different interactions with the graphene and oxide layer are well known. On the oxide surface trapped charged impurities have a tremendous effect on the device characteristics, especially charge carrier mobility. Aluminiumoxides hydrophobia might be an issue for sensing functionalization as the attachment of the interface chemicals might be disfavored.

Future experiments can be done on focusing on the biological interface which provides the sensors specificity. The electrical response of chemical gating through other biomarkers of medical importance, like lyme disease, are of high interest. Further on, control experiments with different antigens than of a matching antibody-antigen complex would be of very high interest.

Residual layers of polymers which occur during the graphene patterning on the graphene field effect transistors are still a major challenge. Developing new patterning methods for graphene and other 2D materials would be a tremendous gain.

Bibliography

[1] Sumio Iijima et al. Helical microtubules of graphitic carbon. *nature*, 354(6348):56–58, 1991.

[2] Kostya S Novoselov, Andre K Geim, SV Morozov, D Jiang, Y₋ Zhang, SV Dubonos, , IV Grigorieva, and AA Firsov. Electric field effect in atomically thin carbon films. *science*, 306(5696):666–669, 2004.

[3] Xuesong Li, Weiwei Cai, Jinho An, Seyoung Kim, Junghyo Nah, Dongxing Yang, Richard Piner, Aruna Velamakanni, Inhwa Jung, Emanuel Tutuc, et al. Large-area synthesis of high-quality and uniform graphene films on copper foils. *Science*, 324(5932):1312–1314, 2009.

[4] Cecilia Mattevi, Hokwon Kim, and Manish Chhowalla. A review of chemical vapour deposition of graphene on copper. *Journal of Materials Chemistry*, 21(10):3324–3334, 2011.

[5] Song Liu and Xuefeng Guo. Carbon nanomaterials field-effect-transistor-based biosensors. *NPG Asia Materials*, 4(8):e23, 2012.

[6] F Schedin, AK Geim, SV Morozov, EW Hill, P Blake, MI Katsnelson, and KS Novoselov. Detection of individual gas molecules adsorbed on graphene. *Nature materials*, 6(9):652–655, 2007.

[7] Mitchell B Lerner, Felipe Matsunaga, Gang Hee Han, Sung Ju Hong, Jin Xi, Alexander Crook, Jose Manuel Perez-Aguilar, Yung Woo Park, Jeffery G Saven, Renyu Liu, et al. Scalable production of highly sensitive nanosensors based on graphene functionalized with a designed g protein-coupled receptor. *Nano letters*, 14(5):2709–2714, 2014.

[8] G Gruner. Carbon nanotube transistors for biosensing applications. *Analytical and bioanalytical chemistry*, 384(2):322–335, 2006.

[9] Philip Richard Wallace. The band theory of graphite. *Physical Review*, 71(9):622, 1947.

[10] Rainer Waser. *Nanoelectronics and information technology.* John Wiley & Sons, 2005.

[11] Phaedon Avouris. Graphene: electronic and photonic properties and devices. *Nano letters*, 10(11):4285–4294, 2010.

[12] Mahdi Pourfath and Hans Kosina. Electronic bandstructure. Lecture notes, 2015. Advanced Course in Quantum Electronics.

[13] Andre K Geim and Konstantin S Novoselov. The rise of graphene. *Nature materials*, 6(3):183–191, 2007.

[14] KSA Novoselov, Andre K Geim, SVb Morozov, Da Jiang, MIc Katsnelson, IVa Grigorieva, SVb Dubonos, and AAb Firsov. Two-dimensional gas of massless dirac fermions in graphene. *nature*, 438(7065):197–200, 2005.

[15] J-H Chen, C Jang, S Adam, MS Fuhrer, ED Williams, and Masa Ishigami. Charged-impurity scattering in graphene. *Nature Physics*, 4(5):377–381, 2008.

[16] Chintamani Nagesa Ramachandra Rao and Ajay K Sood. *Graphene: synthesis, properties, and phenomena.* John Wiley & Sons, 2013.

[17] SV Morozov, KS Novoselov, MI Katsnelson, F Schedin, DC Elias, JA Jaszczak, and AK Geim. Giant intrinsic carrier mobilities in graphene and its bilayer. *Physical review letters*, 100(1):016602, 2008.

[18] Tsuneya Ando. Screening effect and impurity scattering in monolayer graphene. *Journal of the Physical Society of Japan*, 75(7):074716, 2006.

[19] EH Hwang, S Adam, and S Das Sarma. Carrier transport in two-dimensional graphene layers. *Physical Review Letters*, 98(18):186806, 2007.

[20] MI Katsnelson and AK Geim. Electron scattering on microscopic corrugations in graphene. *Philosophical Transactions of the Royal Society of London A: Mathematical, Physical and Engineering Sciences*, 366(1863):195–204, 2008.

[21] Seyoung Kim, Junghyo Nah, Insun Jo, Davood Shahrjerdi, Luigi Colombo, Zhen Yao, Emanuel Tutuc, and Sanjay K Banerjee. Realization of a high mobility dual-gated graphene field effect transistor with al2o3 dielectric. *arXiv preprint arXiv:0901.2901*, 2009.

[22] Adalbert Prechtl. *Vorlesungen über die Grundlagen der Elektrotechnik*, volume 1. Springer Wien New York, 2nd edition, 2007.

[23] T Mueller, F Xia, M Freitag, J Tsang, Ph Avouris, et al. Role of contacts in graphene transistors: A scanning photocurrent study. *Physical Review B*, 79(24):245430, 2009.

[24] GAKPA Giovannetti, PA Khomyakov, G Brocks, VM vd Karpan, J Van den Brink, and PJ Kelly. Doping graphene with metal contacts. *Physical Review Letters*, 101(2):026803, 2008.

[25] B Huard, N Stander, JA Sulpizio, and D Goldhaber-Gordon. Evidence of the role of contacts on the observed electron-hole asymmetry in graphene. *Physical Review B*, 78(12):121402, 2008.

[26] Website. Website, 2016. Available through `http://2015.igem.org/wiki/images/3/35/PRbg_3.png`; opened on June, 6th 2016.

[27] Michael M Cox et al. *Lehninger principles of biochemistry*. Freeman, 2008.

[28] Gerard J Tortora, Berdell R Funke, and Christine L Case. *Microbiology: An Introduction*. Pearson, 2013.

[29] Libo Gao, Wencai Ren, Huilong Xu, Li Jin, Zhenxing Wang, Teng Ma, Lai-Peng Ma, Zhiyong Zhang, Qiang Fu, Lian-Mao Peng, et al. Repeated growth and bubbling transfer of graphene with millimetre-size single-crystal grains using platinum. *Nature communications*, 3:699, 2012.

[30] Yaping Dan, Ye Lu, Nicholas J Kybert, Zhengtang Luo, and AT Charlie Johnson. Intrinsic response of graphene vapor sensors. *Nano letters*, 9(4):1472–1475, 2009.

[31] Steven H Simon. *The Oxford solid state basics.* Oxford University Press, 2013.

[32] AC Ferrari, JC Meyer, V Scardaci, C Casiraghi, Michele Lazzeri, Francesco Mauri, S Piscanec, Da Jiang, KS Novoselov, S Roth, et al. Raman spectrum of graphene and graphene layers. *Physical review letters*, 97(18):187401, 2006.

[33] Nicholas J Kybert, Gang Hee Han, Mitchell B Lerner, Eric N Dattoli, Ali Esfandiar, and AT Charlie Johnson. Scalable arrays of chemical vapor sensors based on dna-decorated graphene. *Nano Research*, 7(1):95–103, 2014.

[34] Christopher A Hunter and Jeremy KM Sanders. The nature of. pi.-. pi. interactions. *Journal of the American Chemical Society*, 112(14):5525–5534, 1990.

[35] Stefan Kubik. Intermolekulare wechselwirkungen. Website, 2016. Available through `https://www.chemie.uni-kl.de/fachrichtungen/oc/kubik/index.php?lan=de&sca=la&lev1=0tea&lev2=oc9&lev3=wec`; opened on May, 12th 2016.

[36] Charles E Mortimer, Ulrich Müller, and Johannes Beck. *Chemie: Das Basiswissen der Chemie.* Georg Thieme Verlag, 2014.